SECTION II. TASK 2. SUBMODEL DEVELOPMENT AND EVALUATION

Objectives

The objectives of this task are to develop or adapt advanced physics and chemistry submodels for the reactions of coal in an entrained-bed and a fixed-bed reactor and to validate the submodels by comparison with laboratory scale experiments.

Task Outline

The development of advanced submodels for the entrained-bed and fixed-bed reactor models will be organized into the following categories: a) Coal Chemistry (including coal pyrolysis chemistry, char formation, particle mass transfer, particle thermal properties, and particle physical behavior); b) Char Reaction Chemistry at high pressure; c) Secondary Reactions of Pyrolysis Products (including gas-phase cracking, soot formation, ignition, char burnout, sulfur capture, and tar/gas reactions); d) Ash Physics and Chemistry (including mineral characterization, evolution of volatile, molten and dry particle components, and ash fusion behavior); e) Large Coal Particle Effects (including temperature, composition, and pressure gradients and secondary reactions within the particle, and the physical effects of melting, agglomeration, bubble formation and bubble transport; f) Large Char Particle Effects (including oxidation); g) SO_x-NO_x Submodel Development (including the evolution and oxidation of sulfur and nitrogen species); and h) SO_x and NO_x Model Evaluation.

II.A. SUBTASK 2.a. - COAL TO CHAR CHEMISTRY SUBMODEL DEVELOPMENT AND EVALUATION

Senior Investigators - David G. Hamblen and Michael A. Serio
Advanced Fuel Research, Inc.
87 Church Street, East Hartford, CT 06108
(203) 528-9806

Objective

The objective of this subtask is to develop and evaluate, by comparison with laboratory experiments, an integrated and compatible submodel to describe the organic chemistry and physical changes occurring during the transformation from coal to char in coal conversion processes.

Accomplishments

Work continued on examining a percolation theory approach instead of Monte Carlo for doing the network decomposition calculations in order to increase computational speed. Using percolation theory, we can get comparable predictions of the tar and gas rates. For the same set of bridge breaking parameters, there are some slight differences in the shape of the tar peak and in the fluidity predictions. The fluidity predictions appear to be the most sensitive to the choice of percolation theory over the Monte Carlo approach, as the definition of the fluid fraction is model dependent.

Work also continued on the incorporation of rank dependent pyrolysis kinetic rates. We have completed a first round of fits to the TG-FTIR data obtained from all eight Argonne coals at four different heating rates and the fluidity data obtained for six of the coals at one heating rate. This procedure provides a set of rank dependent kinetic parameters for gas evolution (CH_4, CO_2) and the breaking of weak bridges (required for tar evolution). For the lower rank coals, we still need to get better resolution of the paraffin/olefin peak from the main tar peak in order to determine the rank dependent parameters. The next step is to try this set of kinetic parameters in the percolation theory version of the model in order to arrive at a consistent set and to complete the work on the other major gas species (CO, H_2O, H_2).

Work continued on the particle swelling model. Additional sets of equations were examined to describe the driving force for swelling and one was chosen which we feel is the most consistent with the physics. Work was also done to solve some numerical problems which make the predictions sensitive to the choice of the time step. It is planned to obtain additional swelling data, to find more relevant data on the gas diffusivity and to make some measurements of pore wall thickness.

Percolation Theory Version of FG-DVC

Work continued on examining a percolation theory approach instead of Monte Carlo for doing the network decomposition calculations. Using percolation theory, we can get comparable predictions of the tar and gas rates. For the same set of bridge breaking parameters, there are some differences in the shape of the tar peak and in the fluidity predictions. This may result from starting with a different lattice configuration. This can be fixed by making slight adjustments in the crosslinking efficiency and in either the vaporization law or the bridge-breaking rate. For the time being, we have chosen to adjust the latter by a factor of two. The fluidity predictions appear to be the most sensitive to the choice of percolation theory over the Monte Carlo approach, as the definition of the fluid fraction is model dependent.

Work also continued on the incorporation of rank dependent pyrolysis kinetic rates, as discussed below. Our approach is to obtain a complete set of kinetic parameters which agree with the volatile evolution and fluidity data using the Monte Carlo method for the eight Argonne coals. Then we will switch to the percolation theory, using the kinetic parameters obtained from the Monte Carlo method as a first approximation in order to arrive at a consistent set and to complete the work on the other major gas species (CO, H_2O, H_2). Finally, the polymethylenes will be added to the percolation theory version as a final adjustment to the predictions.

Rank Dependent Kinetic Parameters

We have completed a first round of fits to the TG-FTIR data obtained from all eight Argonne coals at four different heating rates and the fluidity data

obtained for six of the coals at one heating rate. This procedure provides a set of rank dependent kinetic parameters for gas evolution (CH_4, CO_2) and the breaking of weak bridges (required for tar evolution). The details are discussed below.

Experimental

Pyrolysis experiments were done with the Argonne premium coals at heating rates of 3, 30, 50, and 100°C/min up to 900°C in a TGA with FT-IR analysis of evolved products (TG-FTIR). The TG-FTIR apparatus consists of a sample suspended from a balance in a gas stream within a furnace. As the sample is heated, the evolving tars and gases are carried out of the furnace directly into a 5 cm diameter gas cell (heated to 150°C) for analysis by FT-IR. With this geometry under low heating rate conditions, the temperature of the sample is assumed to be the same as that of a thermocouple which is next to the sample. The TG-FTIR system used in the current work is the TG/Plus from Bomem, Inc. The TG/Plus couples a Dupont 951 TGA with a Bomem Michelson 100 FT-IR spectrometer (Carangelo et al., 1987; Whelan et al., 1988).

High heating (- 20,000 K/s) pyrolysis rate measurements were previously made in a heated tube reactor (HTR) with an Illinois No. 6 coal, as described by Solomon et al. (1986). These experiments included in-situ FT-IR diagnostics for measurement of the coal particle temperature. A heat transfer model was developed which provided a good fit to the measured temperature profile (Solomon et al., 1986; Serio et al., 1987). The predictions of the heat transfer model were subsequently input into the FG-DVC pyrolysis model.

Results

The TG-FTIR results for the Pittsburgh Seam coal at three heating rates are given in Fig. II.A-1. The dashed lines are the prediction of the FG-DVC model (Serio et al., 1987; Solomon et al., 1988a; Solomon et al., 1990) while the experimental data are plotted as asterisks connected by solid lines. The left hand set of curves is for the cumulative weight loss from the balance. Superimposed on each of these plots is the time-temperature profile. Except for very low heating rates, the coal is heated first to 150°C for drying before

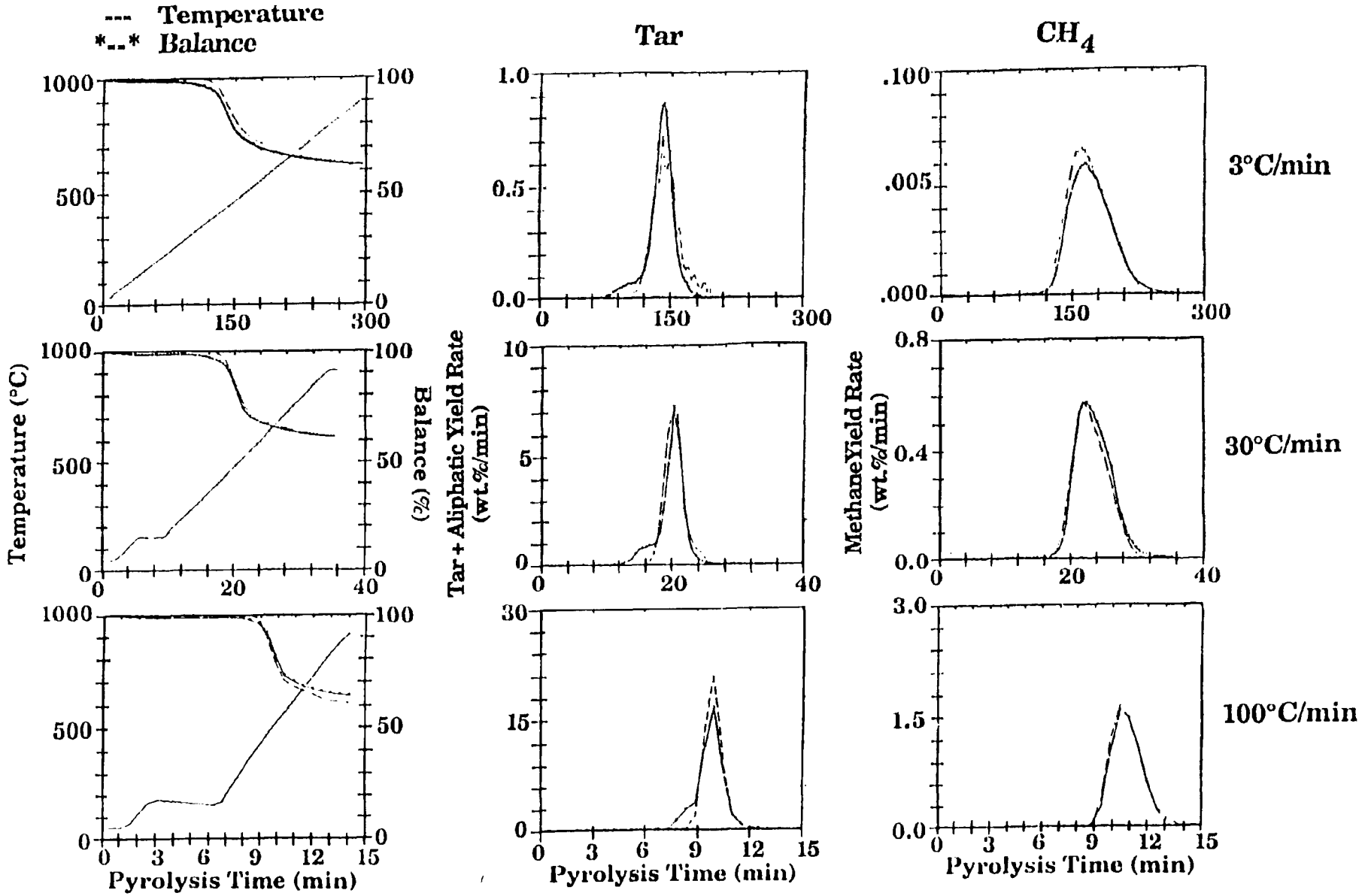

Figure II.A-1. Kinetic Analysis at Three Heating Rates for Pittsburgh Seam Coal. Comparison of Theory (---) and Data (*-*).

heating at the designated rate to 900°C.

The agreement between the experimental and predicted weight predictions is quite good at each of the three heating rates. The predicted weight loss is the sum of the tar evolution and the major gases (CO, CO_2, H_2, H_2O, CH_4, paraffins, olefins) which are included in the FG-DVC model.

The middle set of curves in Fig. II.A-1 is for the tar evolution while the right hand set is for CH_4 evolution. The prediction of tar evolution is based on the breaking of weak linkages between an assumed polymeric structure for coal followed by transport of the molecule out of the coal if it meets the volatility criteria (Solomon et al., 1988a). The position and shape of the main tar peak is predicted very well for the Pittsburgh Seam coal and for several other coals that have been tested. The early part of the tar evolution is not as well predicted. This part of the tar evolution arises primarily from "guest" molecules which are physically bound in the coal. We are working on a new version of the FG-DVC model which includes the quest molecules (Solomon et al., 1990).

The evolution of CH_4, shown on the far right hand side of Fig. II.A-1, is also well predicted. The CH_4 evolution is modeled using two sources which evolve in a manner such that the peaks are usually merged into a single peak (Serio et al., 1987; Solomon et al., 1988a).

Both the tar and CH_4 evolution profiles show a systematic shift with increasing heating rate. The change in the temperature for the maximum evolution rate (T_{max}) with temperature can be used in preliminary analysis to derive kinetic parameters (Juntgen and van Heek, 1968; Braun and Burnham, 1987). We have used this approach to obtain a preliminary estimate of the mean values of the distributed activation energy parameters. The parameters are further refined by using the FG-DVC model to best fit the complete evolution profiles at each of four heating rates. The current set of rank dependent kinetic parameters is given in Table II.A-1.

Similar comparisons are made in Figs. II.A-2 to II.A-5 for other coals in the Argonne series. In this case, the data are shown for a single heating rate

TABLE II.A-1 - RANK DEPENDENT KINETIC PARAMETERS FOR ARGONNE PREMIUM COALS

KINETIC PARAMETERS		COAL							
		ZAP	WYO	ILL	UTAH	LS	PIT	UPF	POC
Bridge Breaking	A	5×10^{15}	4×10^{15}	1.6×10^{13}	5×10^{12}	7×10^{12}	1.3×10^{12}	1.5×10^{12}	3.0×10^{15}
	E/R	30,000	30,000	25,000	25,000	25,000	24,000	25,000	31,000
	σ/R	1,500	1,500	1,250	1,250	1,250	1,250	1,250	1,000
CH_4 Loose	A	7×10^{13}	1.1×10^{14}	1.5×10^{14}	1.5×10^{14}	1.2×10^{14}	1.5×10^{14}	9.5×10^{13}	4.0×10^{13}
	E/R	30,000	30,000	30,000	30,000	30,000	30,000	30,000	30,000
	σ/R	3,000	2,500	2,000	2,000	1,500	1,500	1,000	1,000
CH_4 Tight	A	2.1×10^{12}	8.5×10^{11}	1.9×10^{12}	1.9×10^{12}	2.0×10^{12}	1.9×10^{12}	1.7×10^{12}	1.2×10^{12}
	E/R	30,000	30,000	30,000	30,000	30,000	30,000	30,000	30,000
	σ/R	3,000	2,000	2,000	2,000	2,000	2,000	2,000	1,500
CO_2 X-Loose	A	6.2×10^{12}	2.0×10^{14}	2.0×10^{13}	2.0×10^{13}	8.1×10^{12}	2.0×10^{13}	2.0×10^{13}	1.0×10^{13}
	E/R	22,500	22,500	22,500	22,500	22,500	22,500	22,500	22,500
	σ/R	3,000	3,000	3,000	2,500	1,500	3,600	1,500	3,000
CO_2 Loose	A	1.6×10^{17}	1.3×10^{18}	8.0×10^{17}	1.6×10^{17}	6.5×10^{16}	1.6×10^{17}	1.6×10^{17}	6.5×10^{16}
	E/R	33,850	33,850	33,850	33,850	33,850	33,850	33,850	33,850
	σ/R	3,000	3,000	2,000	2,500	1,500	3,000	3,000	3,000
CO_2 Tight	A	2.1×10^{16}	8.7×10^{15}	1.25×10^{14}	1.0×10^{15}	1.0×10^{16}	5×10^{15}	2.7×10^{15}	1.0×10^{15}
	E/R	38,315	38,315	38,315	38,315	38,315	38,315	38,315	38,315
	σ/R	3,000	3,000	5,000	2,000	2,000	5,000	2,000	1,200

Notes:

A is in units of s^{-1}
E/R is in units of K
σ/R is in units of K

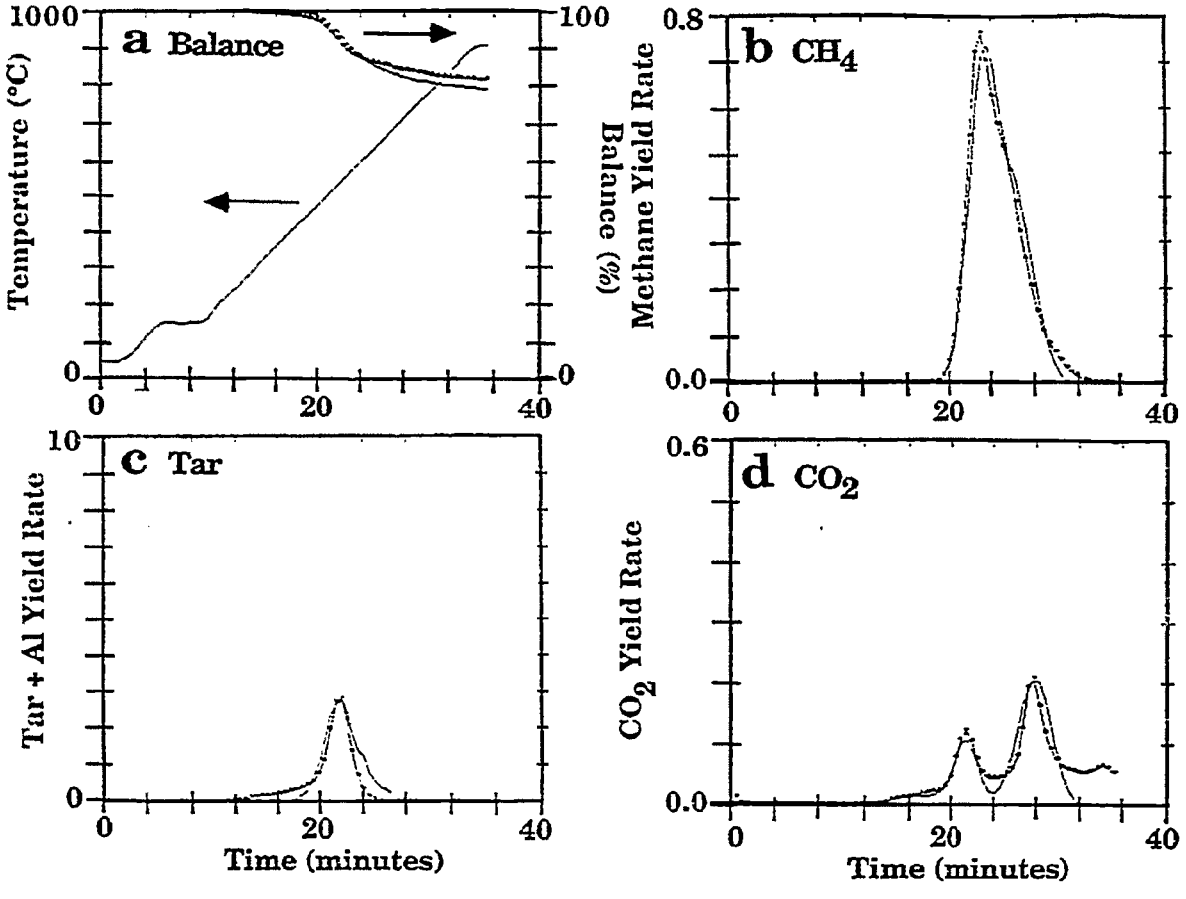

Figure II.A-2. Kinetic Analysis at 30°C/min for Major Volatile Products. Comparison of Theory (---) and Data (*-*) for Pocahontas Coal.

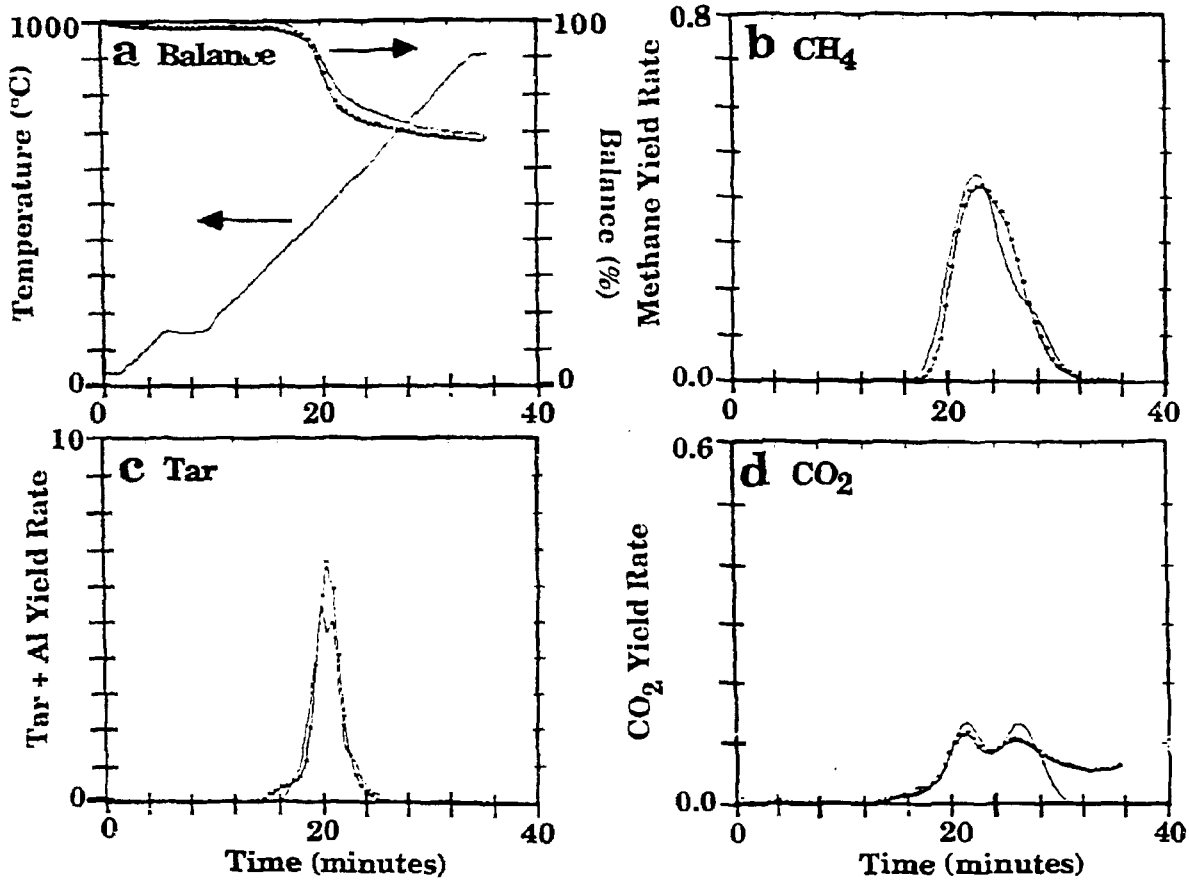

Figure II.A-3. Kinetic Analysis at 30°C/min for Major Volatile Products. Comparison of Theory (---) and Data (*-*) for Lewis-Stockton Coal.

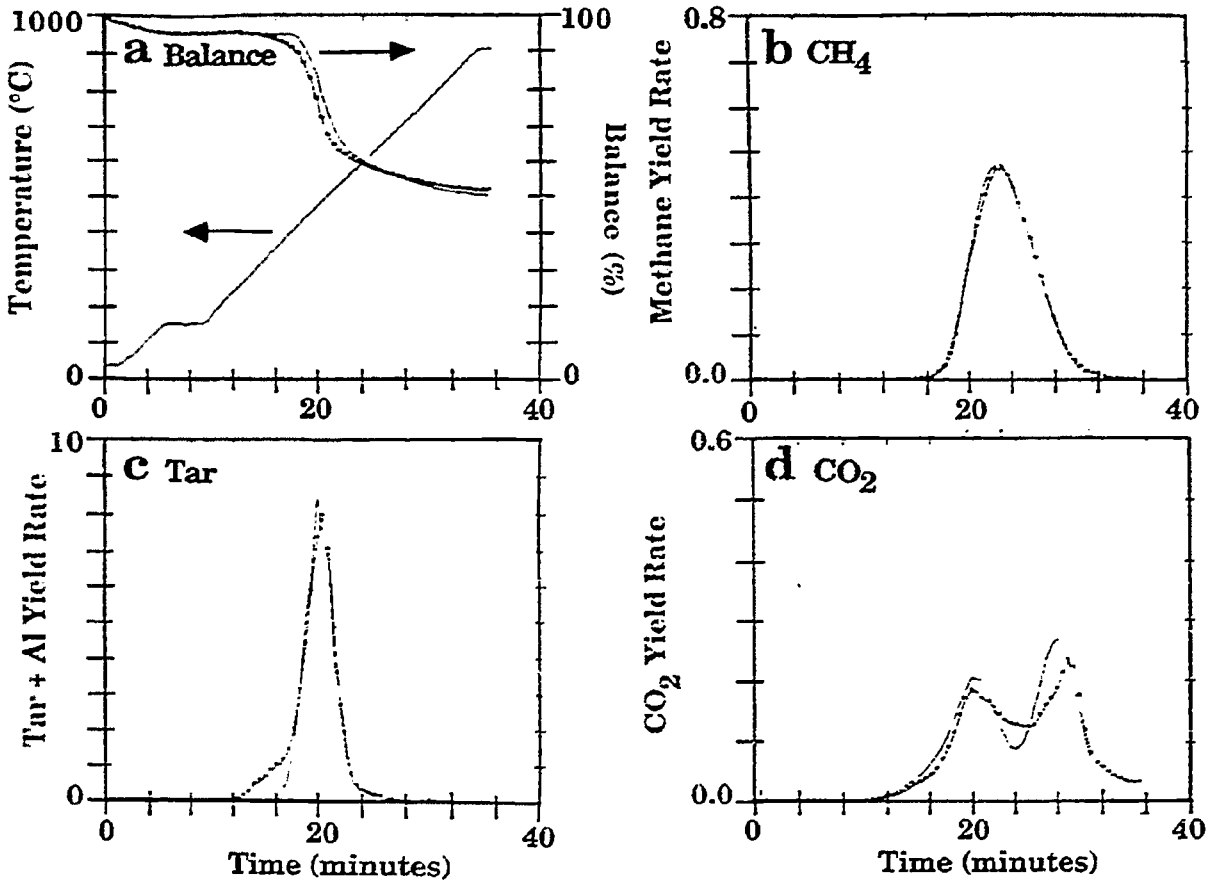

Figure II.A-4. Kinetic Analysis at 30°C/min for Major Volatile Products. Comparison of Theory (---) and Data (*-*) for Utah Blind Canyon Coal.

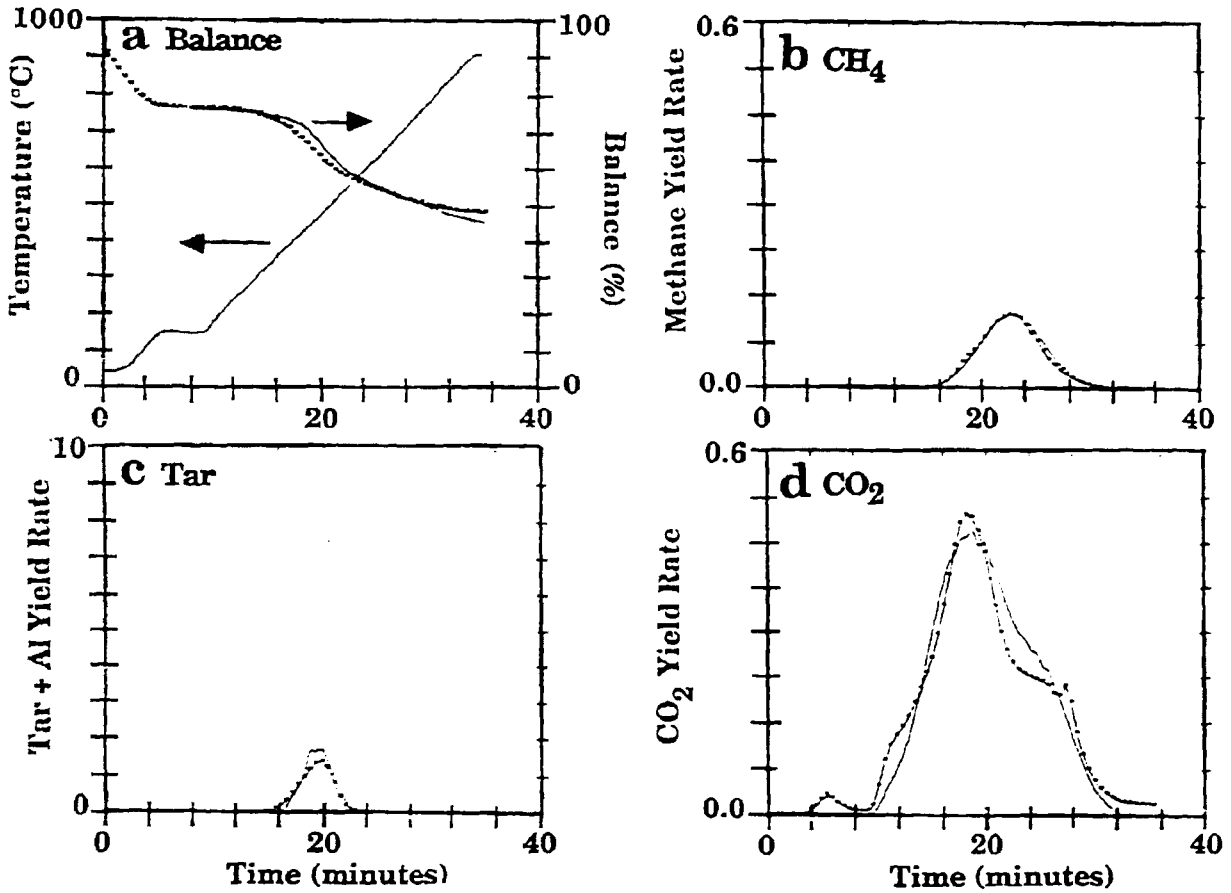

Figure II.A-5. Kinetic Analysis at 30°C/min for Major Volatile Products. Comparison of Theory (---) and Data (*-*) for Zap Lignite

(30°C/min) but one additional species (CO_2). Again, good agreement is obtained for the actual weight loss and the predicted values from all four coals (Figs. II.A-2a to II.A-5a). In the case of the Utah Blind Canyon coal and the Zap lignite, the predicted curves have been horizontally displaced to match the weight loss after moisture evolution since the model predictions are all done on a dry basis.

The predictions of the tar evolution profiles in Figs. II.A-2c to II.A-5c are also good except for the very early tar as discussed above for the Pittsburgh Seam coal. The methane evolution profiles are very well predicted in each case. The CO_2 evolution profiles (Figs. II.A-2d to II.A-5d) are not as well predicted as the evolution of hydrocarbon species. The CO_2 evolution is predicted based on three assumed sources (extra loose, loose, and tight) (Serio et al., 1987; Solomon et al., 1988a). At 30°C/min, the peaks are centered at approximately 16, 22, and 28 minutes, respectively. However, because the mineral sources are not included in the model, the quality of the fits is not the same as for hydrocarbon species where there are no mineral contributions.

Discussion

The use of the TG-FTIR method over a range of heating rates has allowed the development of a set of rank dependent kinetic parameters for tar, CH_4, and CO_2 (and indirectly the weight loss). The parameters for the tar evolution were obtained by adjusting the value of the pre-exponential and activation energy for the bridge breaking rate in the FG-DVC model in order to match the evolution profiles at the four heating rates. In general, these rates increase monotonically with decreasing rank (increasing oxygen content). For very low rank coals, the contribution of polymethylenes is sufficiently large that it partly obscures the tar evolution from bridge breaking. In this case, the TG-FTIR results from demineralized coals are being used to obtain a more reliable estimate of the bridge breaking rate. The lower amount of crosslinking in the demineralized coals reduces the relative contribution of the polymethylene tar. This work is still in progress.

In the case of the CH_4 and the CO_2, good results were obtained by adjusting only the pre-exponential factors. The values of the activation energies used

were the same as those reported previously (Serio et al., 1987; Solomon et al., 1988a).

A good test of the validity of using the TG-FTIR method over a range of low heating rates to obtain kinetic parameters is the ability to use the kinetic parameters to extrapolate to high heating rate conditions. An example of this is shown in Fig. II.A-6, where the parameters obtained for the Illinois No. 6 coal using the TG-FTIR method were used to simulate previously obtained high heating rate (- 20,000 K/s) data for tar evolution (Serio et al., 1987). Again, the agreement between the theory and data is quite good.

Finally, a comparison can be made of results obtained for T_{max} for tar evolution at 3°C/min for the eight Argonne premium coals using the TG-FTIR method with results obtained by Burnham et al. (1989) using a Rock-Eval experiment at 4°C/min. This comparison is shown in Fig. II.A-7. The agreement between the two experiments is generally very good.

Coal Fluidity

The importance of the rank dependence of the pyrolysis kinetics for tar and CH_4 evolution was evident in the modeling of coal fluidity behavior. When modeling fluidity, it was found that relatively small differences in the methane evolution rate (which is related in our model to the moderate temperature crosslinking which shuts down the fluidity) and the tar evolution rate (which is based on the bridge breaking rate as discussed above) have a large effect on the fluidity predictions. In Fig. II.A-8 are shown comparisons of the measured fluidity with the predicted fluidity (based on the rank dependent rates) for five of the eight coals. With the possible exception of the Pocahontas coal, the agreement between the measured and predicted fluidity is quite good.

Plans

The rank dependent parameters will be tested in the percolation theory version of the model and the parameters for the remaining gas species (CO, H_2O, H_2) will be developed. In addition, the work on the swelling model will also be continued. Work will be initiated on studying the evolution of sulfur and nitrogen species.

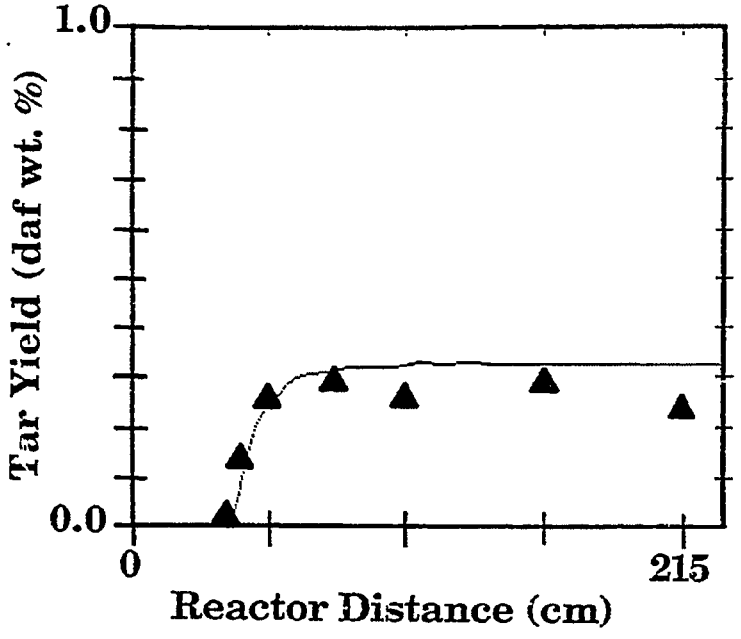

Figure II.A-6. Pyrolysis Tar Yield Results for Illinois No.6 Coal, 200 x 325 mesh, in the HTR at an Equilibrium Tube Temperature of 800°C. The Solid Lines are Predictions of the FG-DVC Model.

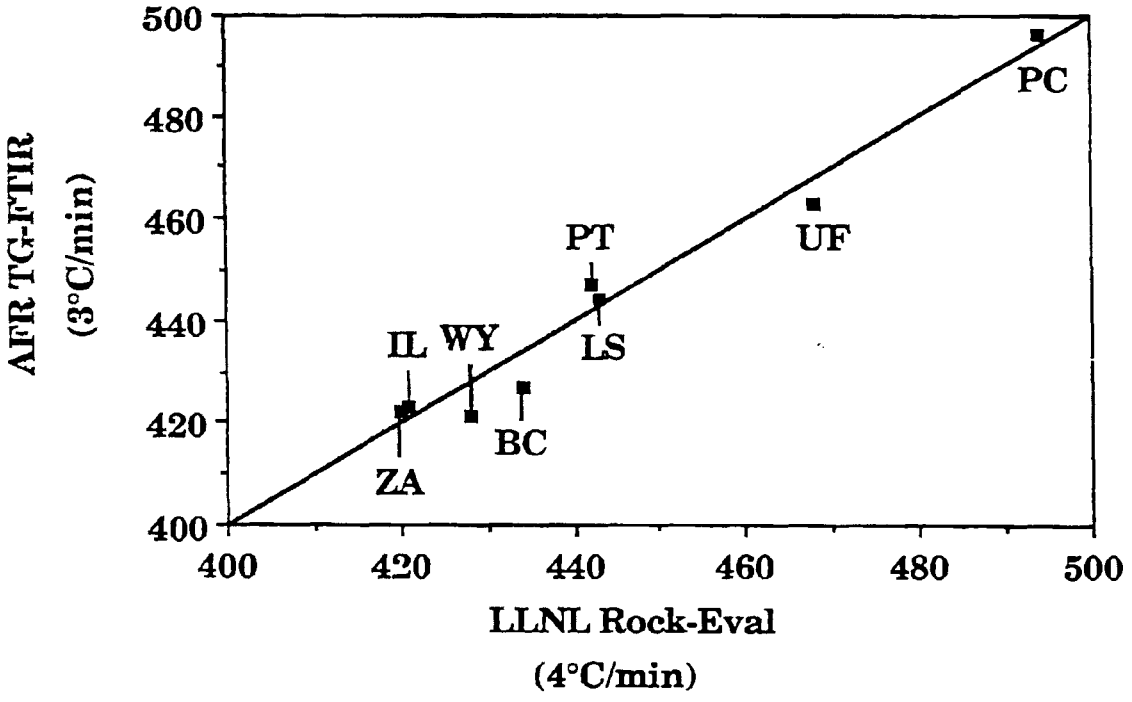

Figure II.A-7. Comparison of AFR Data for T_{max} from TG-FTIR Analysis at 3°C/min with Rock-Eval Data from LLNL at 4°C/min.

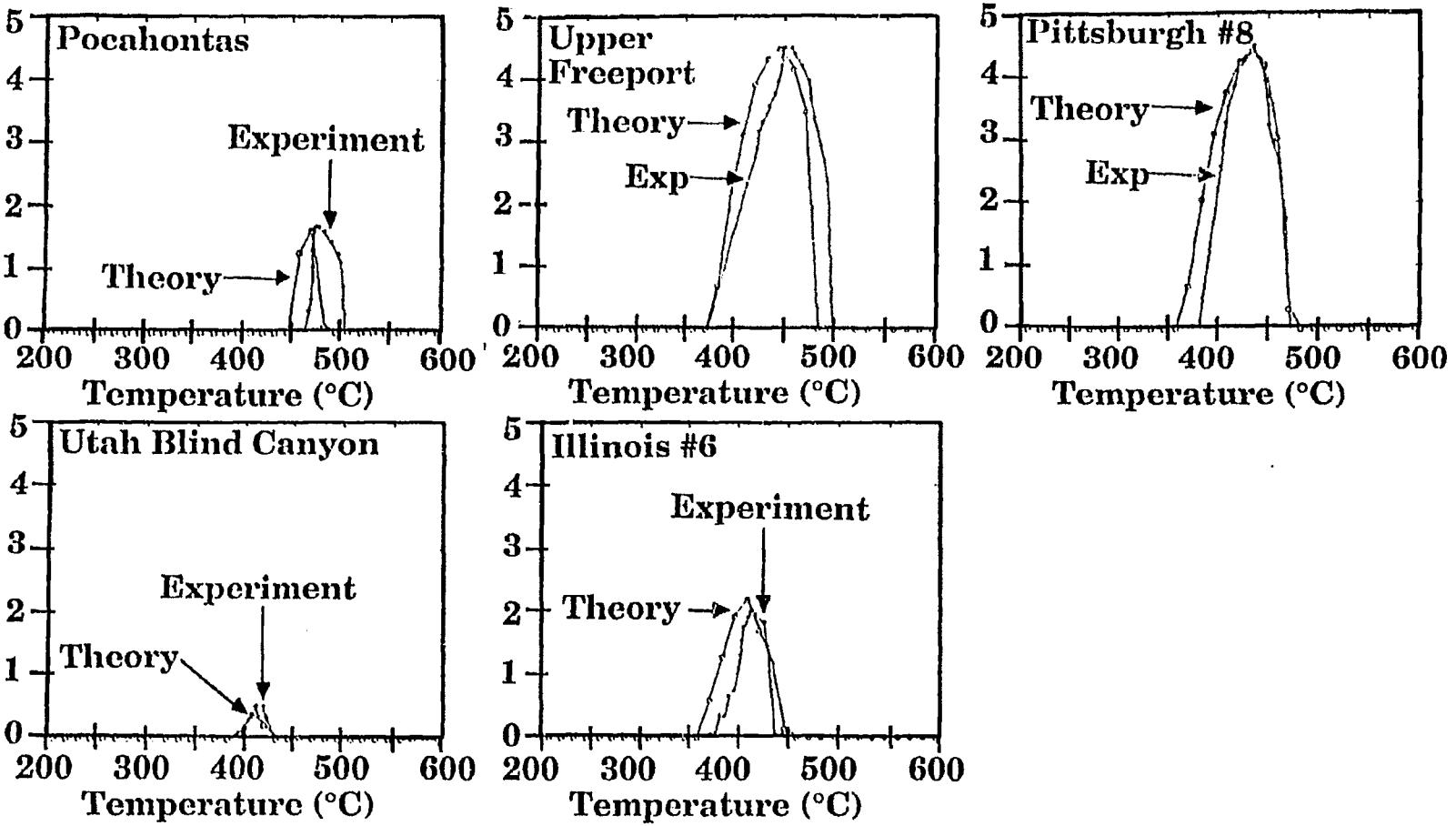

Figure II.A-8. Comparison of Measured (*-*) and Predicted (o-o) Fluidity for Five Argonne Coals.

II.B. SUBTASK 2.B. - FUNDAMENTAL HIGH-PRESSURE REACTION RATE DATA

Senior Investigators - Geoffrey J. Germane and Angus U. Blackham
Brigham Young University
Provo, Utah 84602
(801) 378-2355 and 6536

Student Research Assistants - Charles R. Monson, Gary Pehrson, David Wheeler, and James Rigby

Objective

The overall objective of this subtask is to measure and correlate reaction rate coefficients for pulverized-coal char particles as a function of char burnout in oxygen at high temperature and pressure.

Accomplishments

Three components of this subtask have been identified to accomplish the objectives outlined above: 1) develop the laminar-flow, high-pressure, controlled-profile (HPCP) reactor, 2) prepare char at high temperature and pressure, and 3) determine the kinetics of char-oxygen reactions at high pressure. The HPCP reactor, capable of functioning at 400 psi (27 atmospheres), has been constructed to perform the fundamental reaction rate measurements required for the study. Data from an independent char oxidation study at atmospheric pressure being conducted at BYU will also be used.

Work continued during the last quarter on development of the high-pressure, controlled-profile (HPCP) reactor, the preparation and characterization of char, and the kinetics of char oxidation at high pressure. Most of the effort focused on reactor temperature profile characterization, char size characterization, and oxidation of lignite char. Additional coal devolatilization tests of a coal identified for this study were conducted in connection with an independent research program, which has participated financially in the development of advanced instrumentation for the HPCP.

High Pressure Reactor Development and Characterization

During the initial reactor characterization and char tests, a few modifications were found necessary to improve reactor operation and accuracy of the reactor characterization, which is described below.

Gas Temperature Profile Characterization - In order to obtain accurate gas temperature measurements, a water-cooled, radiation-shielded suction pyrometer was constructed. The probe has a 13-mm outer diameter and 1-meter length. A platinum thermocouple measures gas temperature at the top of the pyrometer. This thermocouple is shielded from radiative heat transfer by two concentric alumina tubes with a mullite honeycomb plug at their upper opening. The gas flow through the pyrometer is measured with a rotameter and regulated with a manual valve. A vacuum pump is used to provide flow at atmospheric pressure. The gas flow is adjusted to obtain an isokinetic condition at the pyrometer entrance to minimize disturbance of the flow field within the reactor.

The suction pyrometer has been used to obtain gas temperature profiles for a number of reactor conditions. Figure II.B-1 shows both gas and reaction tube wall temperatures as functions of axial position under extreme devolatilization conditions. The injection probe was positioned to give a reaction length of 50 cm. The gas temperature is about 150 K lower, but tracks the wall temperature through the length of the reaction zone. The gas temperature rose steeply as the gas entered the reaction zone and fell approximately 400 K in the collection probe. For this test, the gas temperature increased 150 K through the length of the reaction zone. The wall heaters can be adjusted to produce a more nearly isothermal profile.

Figure II.B-2 presents similar data for a char oxidation test with a reaction length of 15 cm. In this case the gas temperature steeply approached the wall temperature at the reaction zone entrance. Gas and wall temperatures were within 20 K of each other through the remainder of the reaction zone, after which the gas temperature fell approximately 400 K in the collection probe. This 400 K temperature drop in the collection probe appears to be sufficient to quench char reactions. The gas temperature tracked the wall temperature much more closely for this configuration because there was sufficient reaction tube length before the reaction zone to heat the secondary gas to the wall temperature.

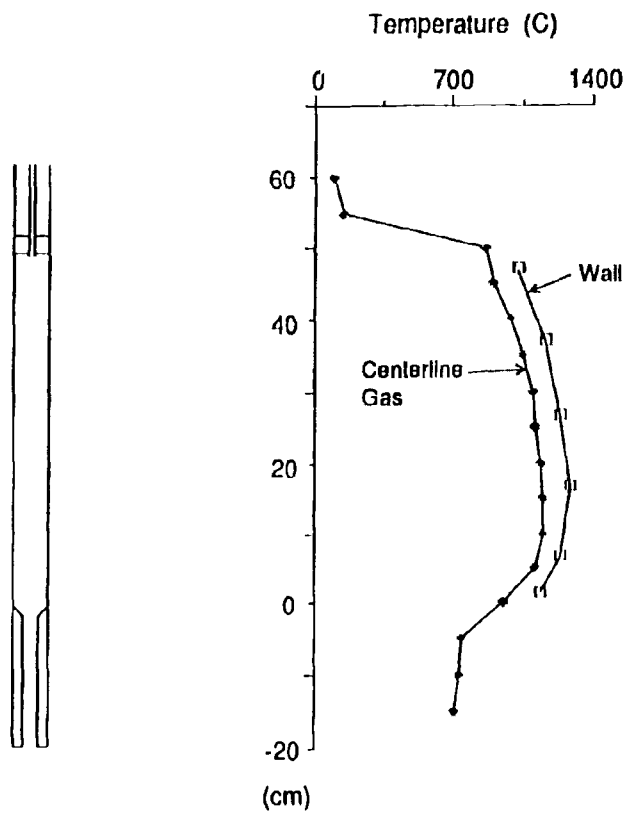

Figure II.B-1. Devolatilization Temperature Profile (ND-P-6)

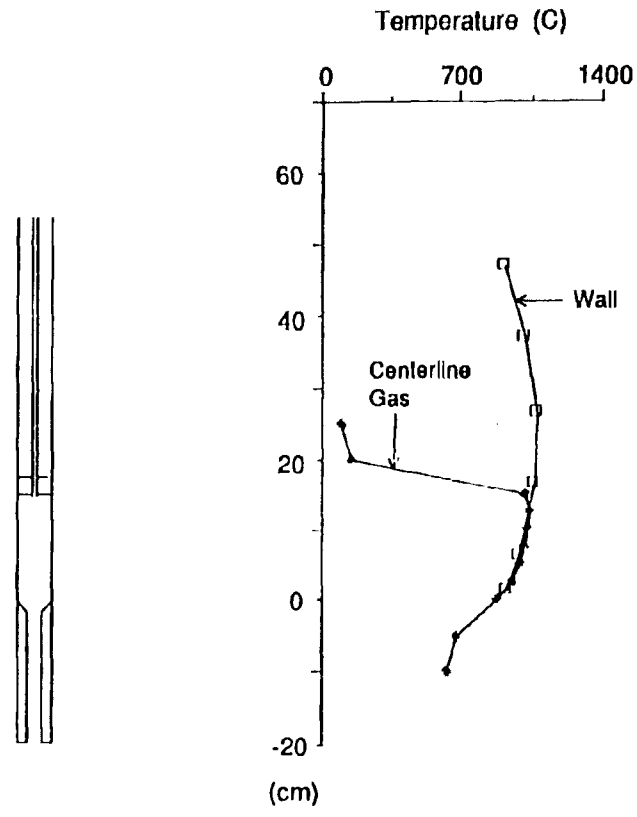

Figure II.B-2. Oxidation Temperature Profile (ND-P-6-2)

Char Injection Probe - A water-cooled injection probe, similar to the original probe but smaller in diameter, was constructed. This new probe has an outer diameter of 9.5 mm compared to an outer diameter of 13 mm for the original probe. The smaller size allows the injection probe to be better insulated, thereby reducing the load on the wall heaters and decreasing the heat loss from the secondary gas as it flows through the reaction tube. The feeder vibrator was relocated from its original position on the feeder carrier assembly to the top of the feeder canister. Vibration of the feeder canister is now isolated from the remainder of the feeder and the reactor by the small, inner feed tubes, which has improved the consistency of particle injection for stickier coal particles.

Optical Instrumentation - The particle imaging system is being assembled. Supports for mounting the optical components have been designed and will be constructed and installed during the next reporting period.

Tar/Char/Gas Collection System - Through independent funding, the collection system of the HPCP reactor was modified to enhance collection efficiency. NMR analyses of previously-collected tar samples revealed differences in the chemical composition of the tars collected through the two collection legs, which suggested that secondary reactions were still occurring after the combustion products had passed through the collection probe. Since qualitative analysis is dependent on accurate definition of reaction parameters, it is critical that all secondary reactions are promptly quenched in the collection probe.

The collection probe was modified to improve the initial quench and an increased quench flow was employed during devolatilization and oxidation runs. Initial NMR analyses of the tars collected in the devolatilization of North Dakota lignite indicate that the tars collected from the two collection legs are consistent in their chemical composition, thus demonstrating that the modifications to the collection probe were effective in reducing secondary reactions.

The virtual impactor was redesigned to increase collection efficiency by reducing recirculation zones and decreasing the internal surface area. The new design will result in a smaller and lighter virtual impactor, and will provide room for the addition of a flow control valve in the char leg between the impactor and cyclone, thus facilitating the collection and removal of char

while the reactor is in operation. In addition, the fitting between the impactor and the collection probe is being redesigned to allow for the attachment of either the virtual impactor or the suction pyrometer.

Char Preparation at High Temperature and High Pressure

Three samples of chars were prepared from a narrowly sized fraction (64-75 μm) of North Dakota lignite at 1720 K and a residence time of 350 ms for the oxidation tests conducted during this reporting period. These are designated ND-P-6, ND-P-7 and ND-P-8 and the char properties are summarized in Table II.B-1. A separate char preparation run (ND-P-9) was also made to provide a tar-char set for NMR analysis for the independently-funded project mentioned previously.

Size analyses of previously-prepared char which had been classified by sieving alone have indicated the presence of small particles of coal below the range of sizes desired. Therefore, samples of North Dakota coal have been both sieved and aerodynamically fractionated to obtain a narrowly sized fraction of the North Dakota coal without the small particles outside the range of sizes intended. Chars were then prepared and analyzed to determine how well the sample would retain the narrow range of particle sizes through the devolatilization process. The range of sizes was determined with both SEM micrographs and Coulter counter particle distributions. One of these char samples (ND-P-8) was then oxidized at three different pressures. Mass reactivities were determined on the basis of both ash content and titanium content.

Figure II.B-3 shows that char prepared from the narrowly sized fraction of coal is reasonably free from particles smaller than 64 μm. Samples ND-P-6 and ND-P-8 are shown at the top and two different particles from ND-P-8 are shown at the bottom. Some of the particles may have increased in size slightly during the devolatilization processes; not much additional porosity is evident. The ND-P-8 sample of char was used for a series of oxidation runs. The char was prepared at 1720 K and 350 ms residence time. These conditions are severe as indicated by the drop in percent hydrogen from 4.8 to 1.0, showing considerable devolatilization.

Coal Particle Sizing - Significant improvements in the quality of size-fractioning of the raw coal have reduced the required time from approximately one week to one day. Using a combination of aerodynamic classifying and

TABLE II. B-1.

CHAR PREPARATION SUMMARY

Sample	Size[1] (μm)	Temp.[2] (K)	Press. (atm)	Res. Time (ms)	Heating Rate (K/s)	%C	%H	%N	Crit. Temp.[3] (K)	SEM (no.)
P8-T-1	64-75	1370	1	44		67.8	3.5	2.3		
P8-T-2	64-75	1370	1	87		66.1	2.8	2.4		
P8-T-3	64-75	1370	1	44		68.1	3.6	2.5		
P8-T-4	64-75	1340	1	92		69.8	1.6	2.8		
P8-T-5	64-75	1340	1	92		70.2	1.3	2.1		
P8-T-6	64-75	1340	1	31		68.7	2.0	2.8		
P8-T-7	64-75	1340	1	31		68.7	2.4	2.4		
P8-T-8	64-75	1340	1	37		73.3	2.3	2.8		
P8-T-9	64-75	1340	1	92		71.0	1.6	2.2		
P8-T-10	64-75	1370	1	26		69.2	4.2	2.3	827	0
P8-T-11	38-43	1300	1	25		71.6	3.5	2.6		0
P8-T-12	64-75	1275	1	17		74.8	4.7	2.4		5
P8-T-13	64-75	1530	9.5	70		74.4	4.5	2.3		1
P8-T-14	64-75	1530	5.1	37		70.0	3.7	2.2		2
P8-T-15	64-75	1530	1	80		72.2	3.2	2.6	850	4
P8-T-16	64-75	1530	1	45		70.5	3.8	2.5		
P8-P-1	64-75	1380	3	257	10^4	65.6	3.1	2.2	817	2
P8-P-2	64-75	1380	1	91	10^4	69.9	3.2	2.4	827	2
P8-P-4	64-75	993	1	860	10^2	71.4	3.7	2.4		0
P8-P-5	64-75	1188	1	786	10^2	70.8	3.3	2.4		5
P8-P-6	64-75	1398	1	685	10^2	70.8	2.7	2.5		0
P8-P-10	64-75	850	1	859	10^2	72.1	4.3	2.4		0
P8-P-11	64-75	1390	1	688	10^2	71.4	2.9	2.4		0
P8-P-12	64-75	993	2.5	3,107	10^2	72.2	2.2	2.7		4
P8-P-13	64-75	993	2.5	2,305	10^2	72.4	2.5	2.9		0
P8-P-14	64-75	743	4.8	3,958	10^2	71.9	3.2	2.4		0
P8-P-15	64-75	839	4.9	4,368	10^2	72.0	3.2	2.6		6
P8-P-16	64-75	953	5.2	4,329	10^2	72.9	3.1	2.6		0
P8-P-17	64-75	998	5.2	4,438	10^2	73.6	2.4	2.8		0
P8-P-18	64-75	1096	5.1	4,604	10^2	73.9	2.4	2.5		0
P8-P-19	64-75	1223	5.4	4,830	10^2	75.1	2.6	2.7		4
P8-P-20	64-75	1388	5.1	3,512	10^2	77.4	1.5	2.5		0
P8-P-21	64-75	1063	10.1	8,822	10^2	77.0	1.3	2.5		0
P8-P-22	64-75	1193	10.1	8,497	10^2	76.5	0.8	2.5		4
P8-P-23	64-75	1480	1	45	10^4	74.2	3.5	2.6		4
P8-P-24	64-75	993	2.7	786	10^2	73.3	3.1	2.5		4

TABLE II. B-1. (continued)

Sample	Size[1] (μm)	Temp.[2] (K)	Press. (atm)	Res. Time (ms)	Heating Rate (K/s)	%C	%H	%N	Crit. Temp.[3] (K)	SEM (no.)
P8-P-25	64-75	993	5	1030	10^2	72.7	4.5	2.5		
P8-P-26	64-75	993	5	1030	10^2	72.1	4.6	2.3		
P8-P-27	64-75	993	1	860	10^2	72.4	4.0	2.2		4
P8-P-28	64-75	993	5	860	10^2	71.1	3.3	2.5		
P8-P-29-A	64-75	1573	1	720	10^4	76.0	0.95	2.5		4
P8-P-29-B	64-75	1573	1	720	10^4	72.9	3.9	2.4		2
ND-P-1	64-75	1570	1	720	10^4	73.0	1.1	1.7		
ND-P-2	64-75	1235	1	50	10^4	62.3	3.8	1.7		
ND-P-3	64-75	1237	1	50	10^4	62.2	3.7	1.5		
ND-P-4	64-75	1141	1	228	10^4	61.9	3.6	1.6		
ND-P-5	64.75	1145	5	224	10^4	63.8	3.4	1.5		
ND-P-6	64-75	1450	1	350	10^4	75.6	1.0	1.5		
ND-P-7	64-75	1450	1	350	10^4	76.4	1.1	1.5		
ND-P-8	64-75	1450	1	350	10^4	78.3	1.0	1.5		
ND-P-9	64-75	1087	1	87	10^4	67.5	3.4	1.6		

1 P8=P.H8 coal; T=hot tube reactor; P=high pressure control profile reactor
2 Coal size fraction, mass mean diameter
3 Calculated particle temperature
4. Measured with TGA
5 P8-P-29-A char fraction <700 μm
P-P-29-B char fraction >700 μm

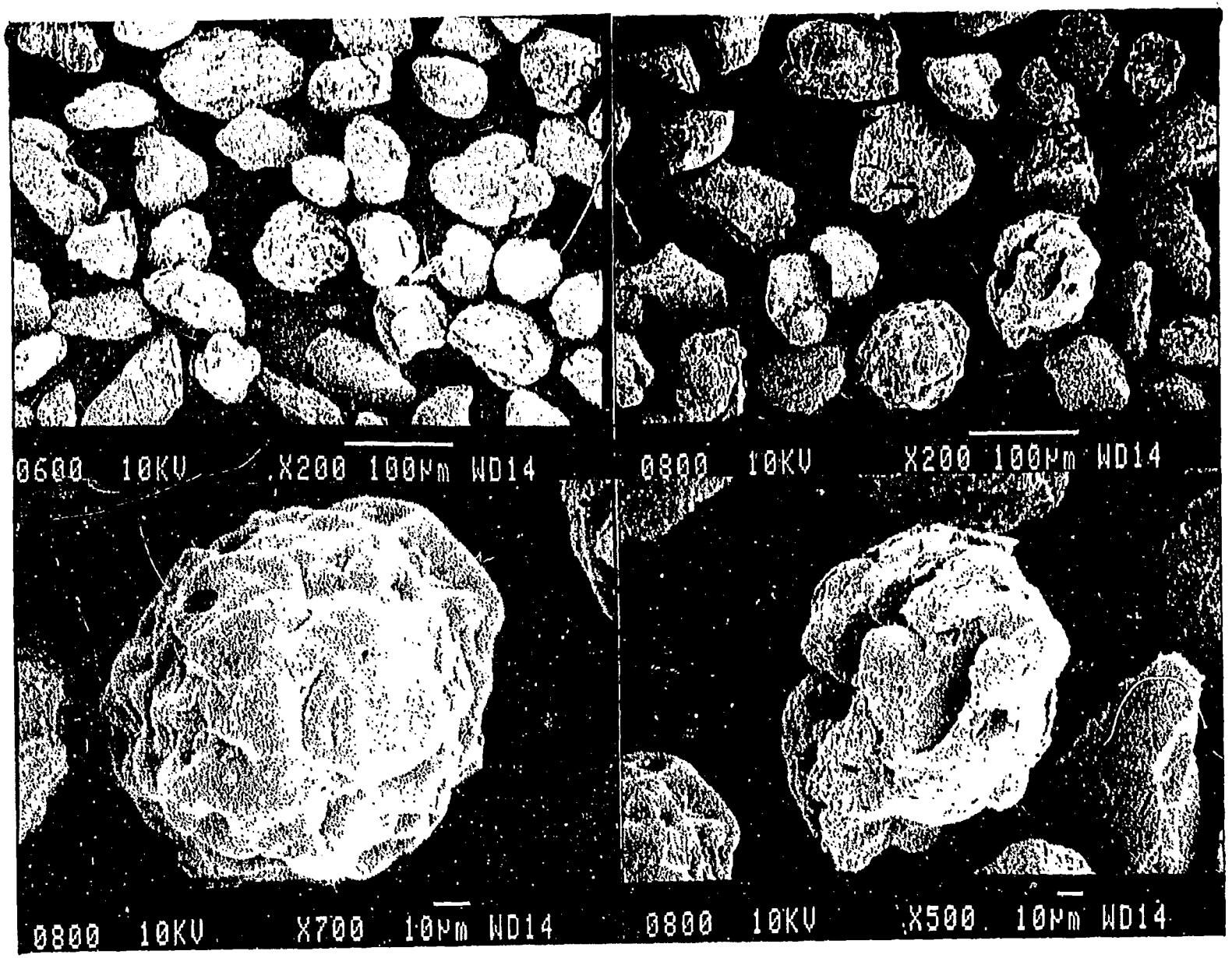

Figure II.B-3. SEM's of devolatilized North Dakota lignite (ND-P-6 -- upper left; ND-P-8 -- others).

sieving. North Dakota coal was sized to a tight fraction with an average diameter of 75 μm. Figure II.B-4 shows a particle size histogram and a scanning electron micrograph (SEM) of the sized coal. Figure II.B-5 presents the same information after devolatilization of the coal. The average particle diameter decreased to 66 μm and the distribution widened somewhat. This is most likely due to softening and rounding of the coal particles as well as some fragmentation during devolatilization.

An aerodynamic particle classifier (Vortec) was implemented to pre-size North Dakota lignite coal particles before sieving them to obtain 64-75 μm particles for char preparation. With the former time-consuming method, the coal was first ground and then sieved with screens. The approach was generalized to size any type of coal to obtain a precise size classification in a relatively short period of time, and is summarized below.

1. Initial Sieving of Pulverized coal.

Purpose: Eliminate particles larger than 500 μm to prevent clogging of the Vortec classifier.

Equipment: 500 μm sieve.

2. Aerodynamic Classification.

Purpose: Separation of coal particles into large and small particle classifications at sizes above and below approximately 50 μm.

Equipment: 1) Vortec classifier at 85 psi and throttle setting of 20. 2) Electrical resistance particle sizer (Coulter counter) with 400 μm aperture to determine the presence of particles greater than 50 μm in the sample of small particles.

Approach/Results: The classifier does not create a sharp size division, but rather particle size rolls off at a certain cut point. For this reason, it was desired that no particles larger than 50 μm be present in the sample of small particles so that particles between 64-75 μm in diameter would not be diverted from the sample of larger particles. The Coulter counter was used to help adjust the size of the particles in the smaller particle size classification through repeated tests at various valve settings until it was verified that no particles larger than 50 μm diameter were present in the sample.

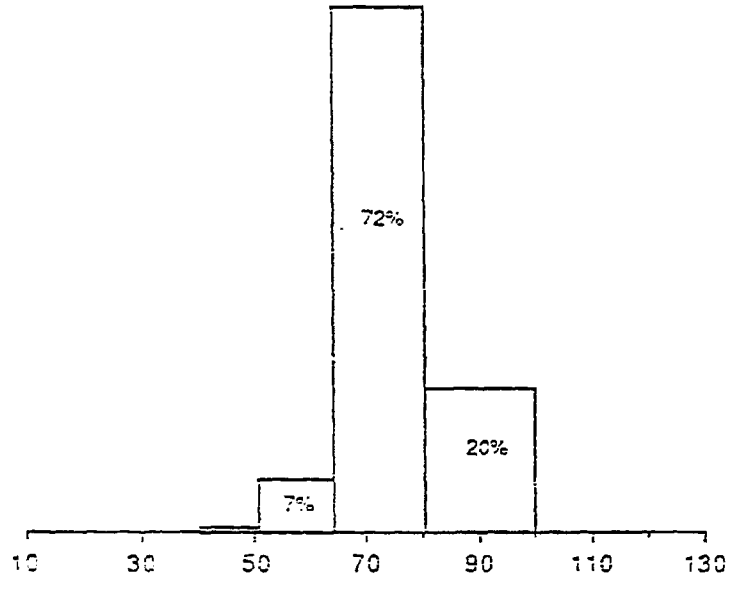

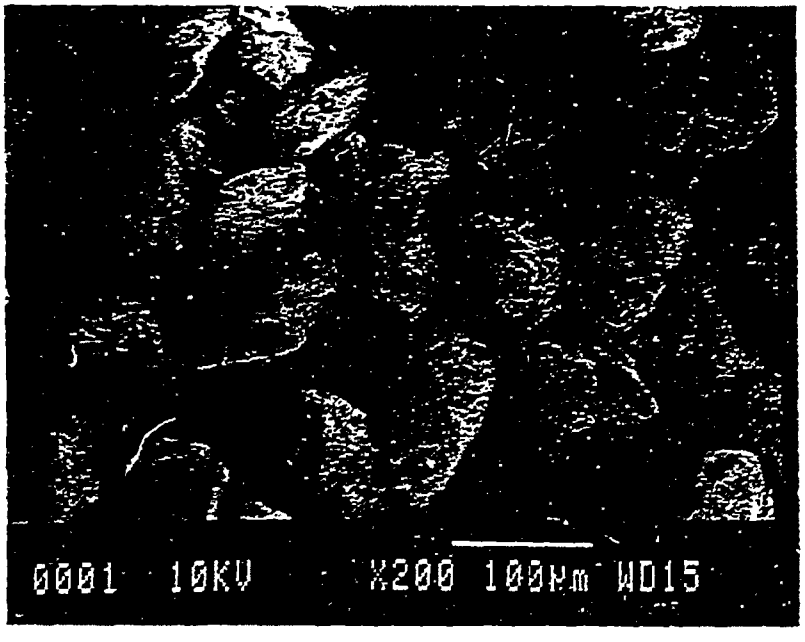

Figure II.B-4. North Dakota Coal (64-75 µm size fraction)

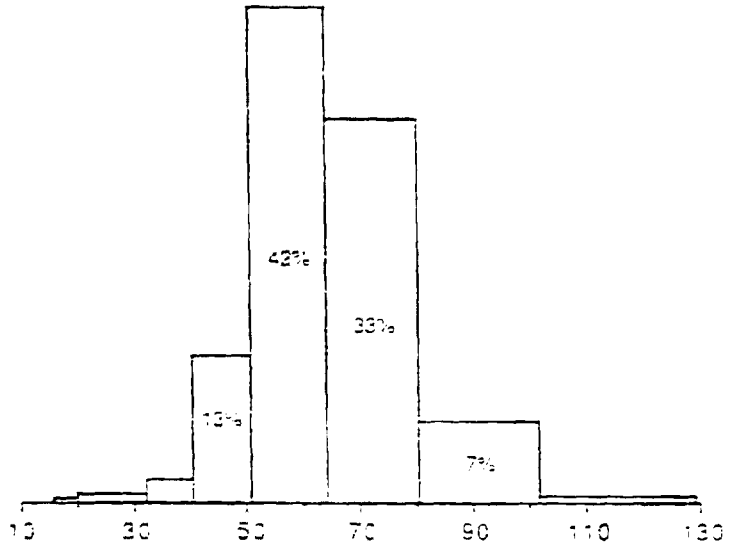

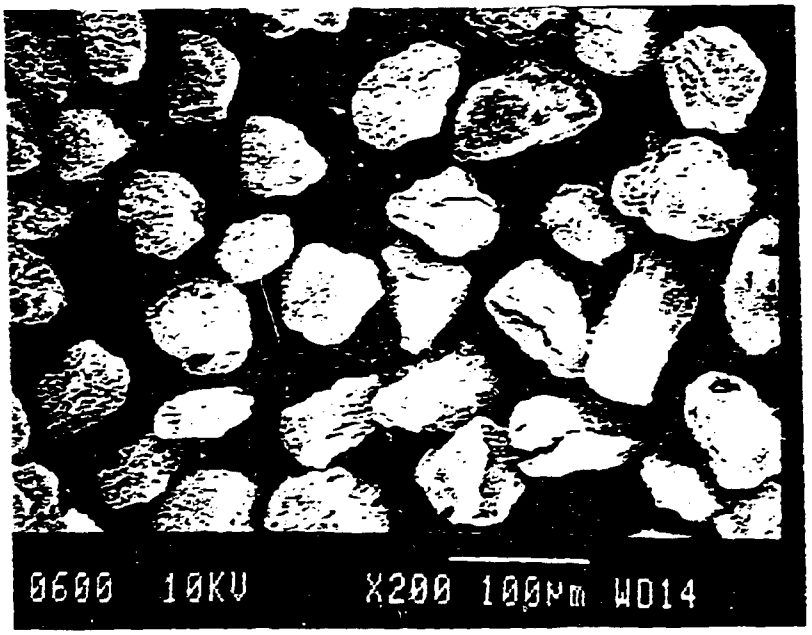

Figure II.B-5. North Dakota Char (ND-P-6)

3. Sieving of large size classification.

Purpose: Narrow size range of large particles

Equipment: Rotary sieve shaker using 250, 150, 125, 106, 75, and 63 μm sieves in descending order.

Approach/Results: Majority of particles collected in the 63 μm sieve were between 64-75 μm.

4. Grinding of large particles.

Purpose: Increase yield of 64-75 μm particles from total char sample.

Equipment: Ball mill grinder

Approach/Results: All particles larger than 75 μm from step 4 and all particles from step 1 were ground for 1 hour to reduce their size. It was found that grinding for 1 hour was the optimal time to reduce the particle size without producing a large amount of unusable particles smaller than 50 μm.

Table II.B-2 shows the improvement in size classification achieved with the aerodynamic separator, resulting in significant time savings and effectiveness. The percentages were obtained with the Coulter counter with a 400 μm diameter aperture. Examination of the scanning electron micrograph of the sample prepared with the "new" method in Figure IIB-4 shows that there are particles in the sample of irregular shape which have volumes greater than 64-75 mm diameter spherical particles. The micrograph also shows that the particles in the sample are fairly close in size and that the oblong particles may not be much larger in actual volume than the more spherical particles in the sample.

Even with these improvements, the desired size range of exclusively 64-75 mm diameter particles cannot be perfectly achieved, since coal particles are generally oblong and irregularly shaped. For this reason, particles whose volume may be greater than that of a spherical 64-75 μm diameter particle were present in the particles which accumulated in the 63 μm mesh sieve. These larger particles slipped through the larger mesh and collected in the 63 μm

Table II.B-2.

COMPARISON OF SIZE DISTRIBUTION OF FOR "OLD" AND "NEW" PARTICLE SIZING METHODS FOR DESIRED RANGE OF 64-75 μm DIAMETER PARTICLES.

Size Range (μm diameter)	**Old Method** (Sieving and grinding only, % of total)	**New Method** (with Vortec, % of total)
16 - 20.2	2.3	2.9
20.3 - 25.4	1.6	0.9
25.4 - 32.0	2.8	0.3
32.0 - 40.3	2.4	0.4
40.3 - 50.8	19.8	0.9
50.8 - 64.0	37.5	5.9
64.0 - 80.6	17.5	73.4
80.6 - 101.6	10.6	14.6
101.6 - 128	3.5	0.4
128 - 161	--	--
Approx. time required	1 week	1 day

mesh because their smallest dimension may have been between 64-75 μm diameter. This variation is shown in the Coulter counter results for both methods. However, the majority of particles collected on the sieve after classification with the Vortec were within the 64-75 μm diameter size range. Particles smaller than 50 μm were also present, although their total count is less than 10 percent of the sample population; on a mass basis their effect is minimal.

Since the Coulter counter determines particle size based upon cross-sectional area in channels of various size ranges, the volume of individual oblong particles compared with the volume of 64-75 μm particles is probably not as large as it may appear. For the channel which includes 80.6-101.6 μm diameter particles, a particle with a volume equivalent to the volume of a 80.6-μm-diameter sphere is classified in the same channel as a particle with a volume equivalent to a 101.6-μm-diameter sphere. However, it is thought that the majority of particles in the test sample fall closer to the 64-75 μm diameter range.

Kinetics of Char-Oxygen Reactions at High Pressure

During the reporting period, char oxidation experiments were continued with size-fractioned North Dakota lignite coal. Table II.B-3 is a summary of all char oxidation experiments conducted under this study to date. Tests ND-P-6 through ND-P-8 were performed during the reporting period. The newly installed suction pyrometer enabled gas temperatures to be accurately measured. Past reactor operating conditions were duplicated and calculations of particle temperatures were made.

Results from the oxidation test ND-P-6-2 are shown in Figure II.B-6. The average particle diameter decreased to 45 μm and a substantial percentage of the particles are smaller than 20 μm. From the electron microscope, it was determined that the small particles are mainly composed of silicon. It appears that the minerals in the char melted and separated from the char particles, subsequently solidifying as spheres. From the SEMs, it was inferred that a number of particles burned with decreasing density without changing diameter significantly while most particles became smaller in diameter and decreased in density. This indicates that combustion occurred in Zone II, where pore diffusion is significant.

The char from the oxidation run at 1450 K, 95 ms and 1 atm is shown in Figure II.B-7 and is designated ND-P-8-1. Burnout is evident from the change

TABLE II. B-3.

CHAR OXIDATION SUMMARY

Sample	Size[1] (μm)	Pressure (atm)	Particle Temp. (K)	% Oxidizer	Res. Time[2] (ms.)	%C	%H	%N	%Ti	%Ash	% Burnout by Ti	% Burnout by Ash	Mass React. by % Ti (kg/kg·s)	Mass React. by % Ash (kg/kg·s)
I6-G-1	64-75	1		0		63.49	1.14	1.87	0.116	33.5				
I6-G-1-1	64-75	1	1173	21	75	55.94	0.88	1.79	0.171	41.4		19.1	4.2	2.540
I6-G-1-2	64-75	1	1173	21	150	48.91	0.50	1.36	0.173	49.23		32.0	2.2	2.130
I6-G-1-3	64-75	1	1023	21	75	64.40	1.04	1.99	0.116	32.6		--	---	---
I6-G-1-4	64-75	1	1023	21	150	64.04	1.07	1.86	0.120	33.0		--	---	---
P8-T-15	64-75	1	1530	0	80	72.2	3.2	2.6		22.0		--		
P8-T-15-1	64-75	1	1173	21	62	72.5	2.8	2.4	0.0760	22.3		1.30		0.220
P8-T-15-2	64-75	1	1173	21	114	72.0	3.1	2.8	0.0650	22.1		0.5		0.040
P8-T-15-3	64-75	1	1277	21	57	71.8	3.1	2.7	0.0665	22.4		1.8		0.310
P8-T-15-4	64-75	1	1277	21	106	71.7	2.7	2.6	0.0625	23.0		4.3		0.410
P8-T-15-5	64-75	1	1370	21	56	71.2	2.7	2.5	0.0631	23.6		6.8		1.360
P8-T-15-6	64-75	1	1461	21	89	72.5	2.2	2.2	0.0655	23.1		4.8		0.540
P8-P-29-A	<700	1	1420	0	720	76.0	0.95	2.5	0.0560	14.7				
P8-P-29-1	<700	1	1307	21	50	75.0	1.2	2.4	0.0560	15.1	0.0	2.6	0.0	0.530
P8-P-29-2	<700	1	1699	21	100	74.5	0.8	2.6	0.0570	20.4	1.8	28	.175	2.790
P8-P-29-3	<700	1	1636	21	150	74.9	0.7	2.6	0.0550	20.6	--	29	---	1.910
P8-P-29-4	<700	1	1667	21	200	73.6	0.7	2.5	0.0700	26.0	20.4	43	1.0	2.170
P8-P-29-5	<700	1	1710	21	200	68.2	0.5	2.7	0.0890	26.4	37.1	44	1.85	2.220
P8-P-29-6	<700	1	1404	21	200	76.0	0.9	2.3	0.0590	17.9	5.1	18	.254	0.893
P8-P-29-7	<700	1	1502	21	200	76.0	0.8	2.3	0.0830	20.0	32.5	27	1.63	1.330
P8-P-29-8	<700	1	1510	21	200	75.8	0.6	2.3	0.0900	18.2	37.8	19	1.89	0.962
P8-P-29-9	<700	1	1623	21	100	76.0	0.9	2.7	0.0800	19.4	30.0	24	3.0	2.420
P8-P-29-10	<700	1	1553	21	360	72.3	0.62	2.5	0.1190	26.7	52.9	45	1.47	1.250
P8-P-29-11	<700	1	1766	21	200	68.2	0.4	2.3	0.1280	27.3	56.3	46	2.81	2.310
P8-P-29-12	<700	1	1667	21	100	75.1	0.6	2.4	0.0860	17.6	34.9	16	3.49	1.650
P8-P-29-13	<700	5	1580	21	200	72.0	0.6	2.4	0.0790	20.6	29.1	29	1.46	1.430
P8-P-29-14	<700	5	1533	21	100	74.6	0.9	2.3	0.0790	17.7	29.1	17	2.91	1.690
P8-P-29-15	<700	5	1497	21	190	73.7	0.7	2.2	0.0810	20.2	30.9	27	1.62	1.430
ND-P-1	<100	1		0	720	73.0	1.1	1.7	0.0356	15.4				
ND-P-1-1	<100	1	1301	21	100	63.6	0.5	1.6	0.0776	27.0	54.1	43.0	5.412	4.330
ND-P-1-2	<100	1	1411	21	100	34.6	0.1	1.4	0.1641	60.6	78.3	74.6	7.831	7.480
ND-P-1-3	<100	1	1373	21	75	68.1	0.5	1.5	0.0571	24.5	37.7	37.1	5.020	5.010
ND-P-1-4	<100	1	1152	21	50	72.1	1.0	1.5	0.0303	16.5	--	6.7	-	1.450
ND-P-1-5	<100	1	1070	21	50	72.3	1.0	1.5	0.0531	16.0	33.0	3.8	6.591	0.875
ND-P-1-6	<100	1	1085	21	100	72.9	0.8	1.5	0.0391	16.5	9.0	6.7	0.8951	0.727
ND-P-1-7	<100	1		21	200		100% Burnout							
ND-P-6	64-75	1	1430	0	350	--	--	--						
ND-P-6-1	64-75	1	1470	21	100	--	--	--	--	--	--	--	--	--
ND-P-6-2	64-75	1	1500	21	100	--	--	--	--	--	--	--	--	--
ND-P-8	64-75	1	1450	0	350	78.3	1.0	1.5	0.0777	12.5				--
ND-P-8-1	64-75	1	1453	21	95	62.0	0.1	1.4	0.2674	35.3	70.9	64.6	7.47	6.80
ND-P-8-2	64-75	1	1252	21	93	73.8	0.7	1.5	0.087	15.8	10.7	20.9	1.15	2.25
ND-P-8-3	64-75	1	1386	21	95	64.3	0.3	1.4	0.1777	29.9	56.3	58.2	5.92	6.13
ND-P-8-4	64-75	5	1427	21	92	63.0	0.5	1.5	0.1411	28.2	44.9	55.7	4.88	6.05
ND-P-8-5	64-75	5	1311	21	94	70.4	0.7	1.5	0.1176	19.3	33.9	35.2	3.61	3.75
ND-P-8-6	64-75	5	1254	21	93	73.6	0.9	1.5	0.1051	16.6	26.1	24.7	2.80	2.66
ND-P-8-7	64-75	8	1355	21	139	53.4	0.6	1.4	0.2280	34.5	65.9	63.8	4.75	4.59

[1]Char size fraction

[2]Calculated

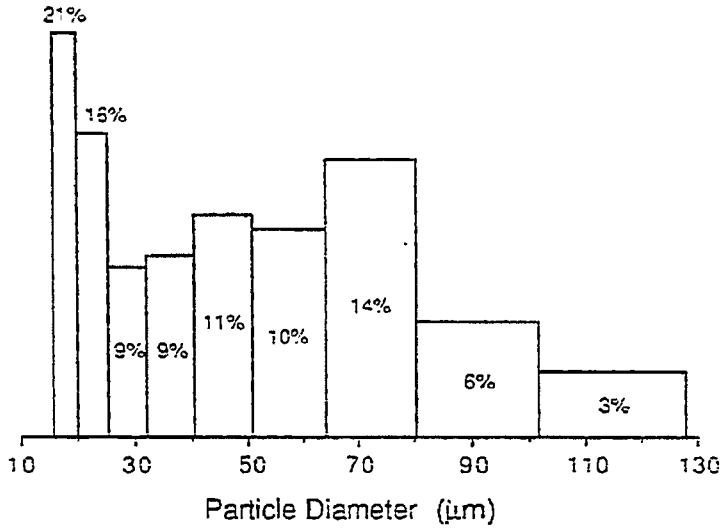

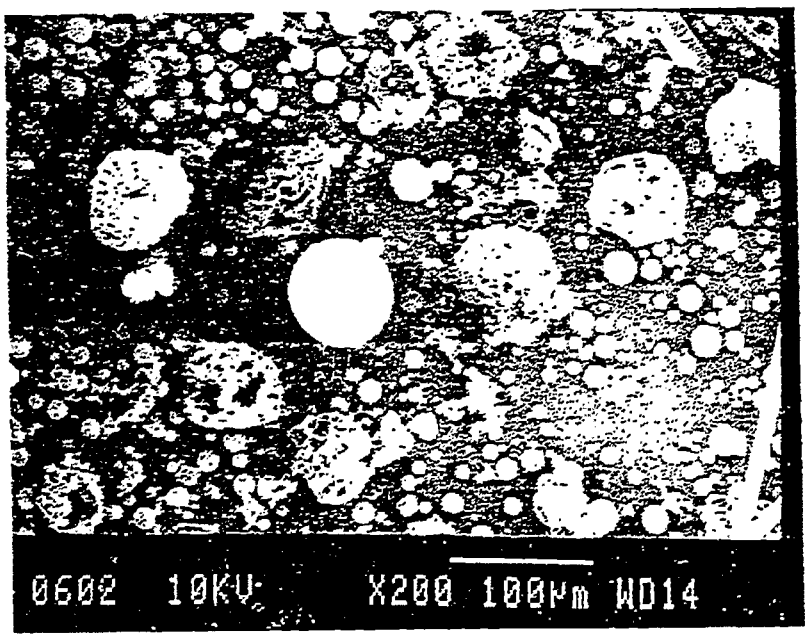

Figure II.B-6. Oxidized North Dakota Char (ND-P-6-2)

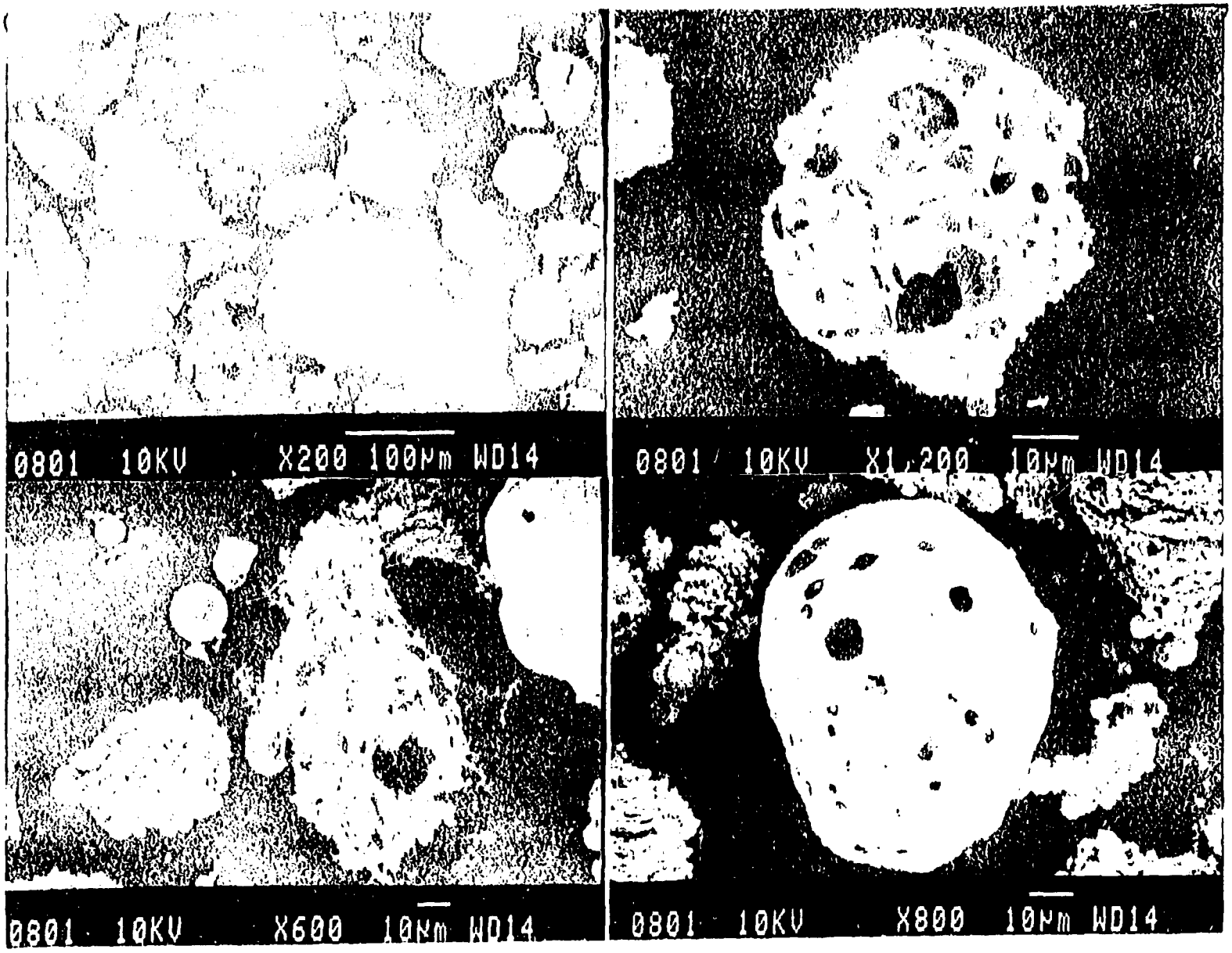

Figure II.B.7 SEM's of oxidized North Dakota lignite char (ND-P-8-1)

in carbon content from 78.3 to 62.0% and from the increased porosity of the particles. Not all particles show a high degree of porosity. Some have a lacy structure, yet others appear not to have reacted significantly at all. Figure II.B-8 shows the sample ND-P-8-2 (upper micrographs) which is oxidized at a lower temperature (1252 K) at the same residence time and pressure. There is less burnout indicated. The carbon content has not decreased as much (78.3% to 73.8%). The majority of the particles appear not to have reacted significantly, and only a few show the lacy structure. The biggest difference in these two samples is in their fragmentation. The ND-P-8-1 sample with the greater burnout has more small particles (<10 μm) than the ND-P-8-2 sample. It appears that fragmentation increases as burnout increases.

The lower micrographs in Figure II.B-3 show sample ND-P-8-4 which was oxidized at a higher temperature (1427 K) and at 5 atmospheres pressure. The appearance is more like the sample ND-P-8-1. More burnout is observed with more fragmentation resulting in small particles (<10 μm).

Figure II.B-9 shows sample ND-P-8-7 oxidized at 1355 K, 139 ms residence time and 8 atmospheres pressure. While the temperature is about one hundred degrees lower, the increase in residence time and pressure result in micrographs of about the same appearance as ND-P-8-1. The percent carbon (53.4%) indicates the most extensive burnout of these samples. The nature of the porosity is different. At the higher pressure, a rough lacy surface is observed for some particles and others seem to have softened to a greater extent under the pressure.

Under each set of conditions, some particles appear to be unreactive, while others that have partly reacted and still others that appear to have reacted completely. This may suggest that some particles start to oxidize, experience a local rise in temperature and then oxidize almost completely before other particles have even started to react. This is consistent with the non-uniform surface appearance of the devolatilized coal particles shown in Figure II.B-5. Some particles appear more porous than others, and some show cracking and evidence of escaped gas, suggesting a variation in char surface characteristics prior to oxidation, which may contribute to the apparent wide variation in characteristics of oxidized particles.

The mass reactivities for all of the chars tested in this study as a function of particle temperature determined by ash as a tracer are shown in Figure II.B-10. The best fit through the Pittsburgh #8 char reactivity data

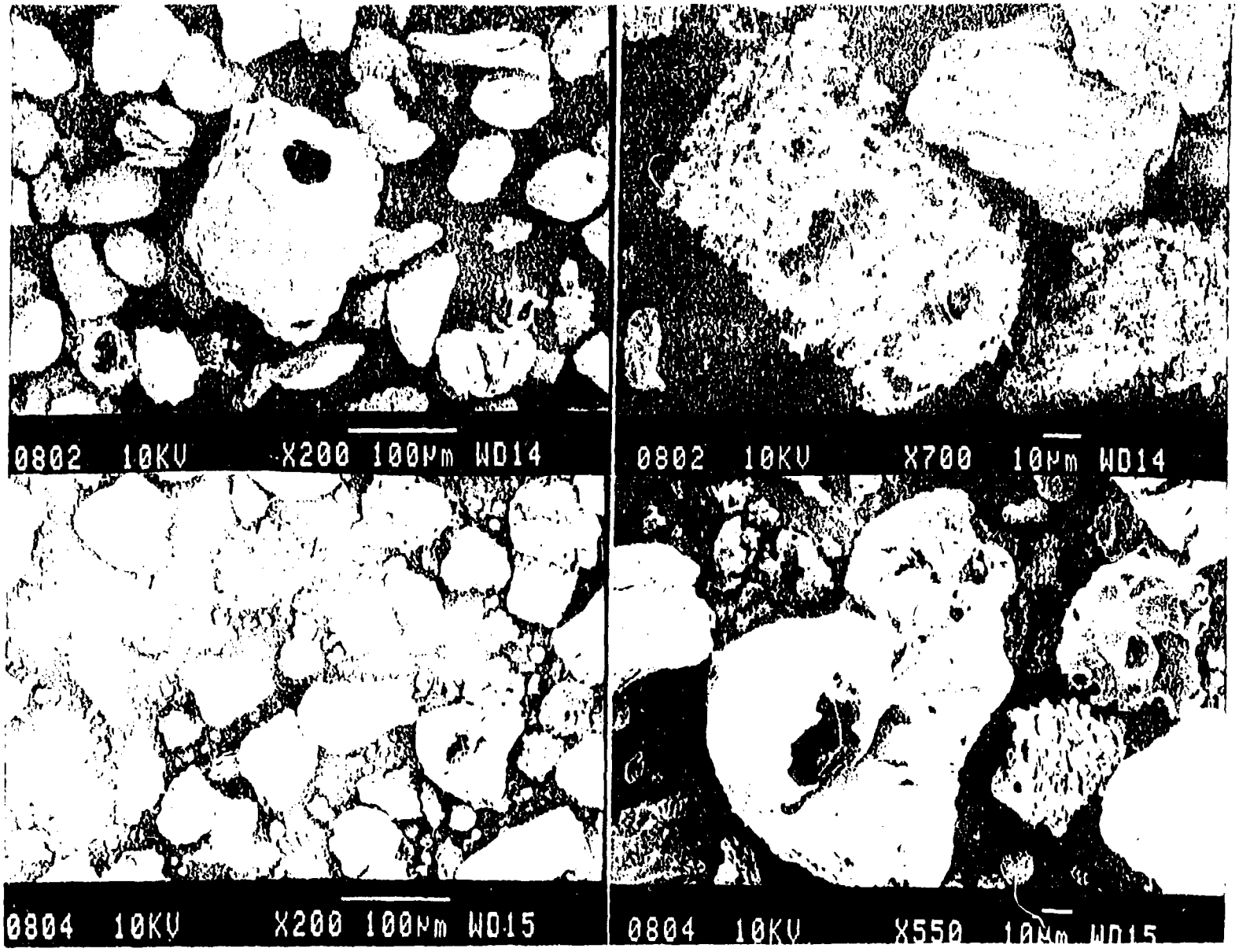

Figure II.B-8. SEM's of oxidized North Dakota lignite chars (ND-P-8-2 -- upper; ND-P-8-4 -- lower).

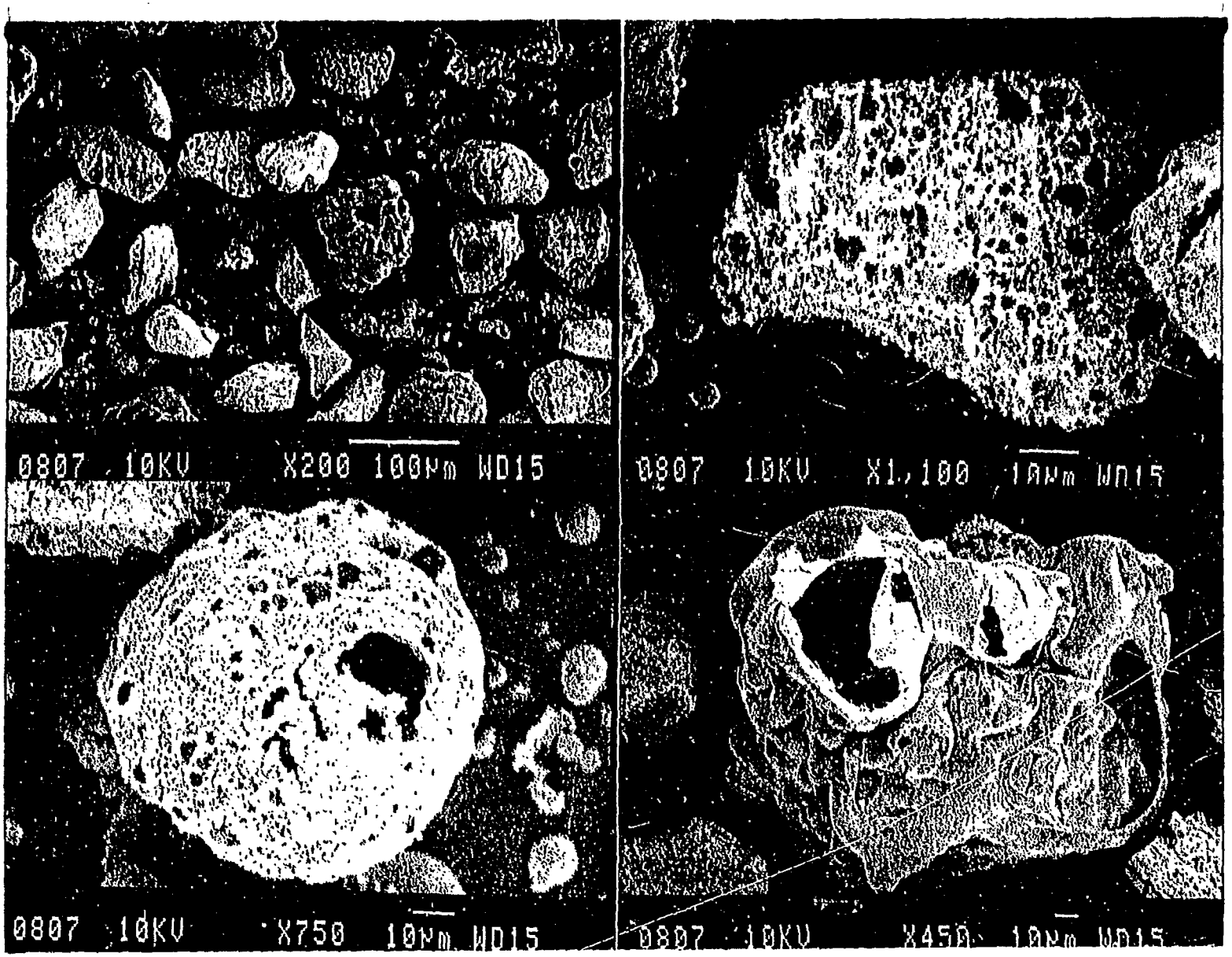

Figure II.B-9. SEM's of oxidized North Dakota lignite char, sample ND-P-8-7.

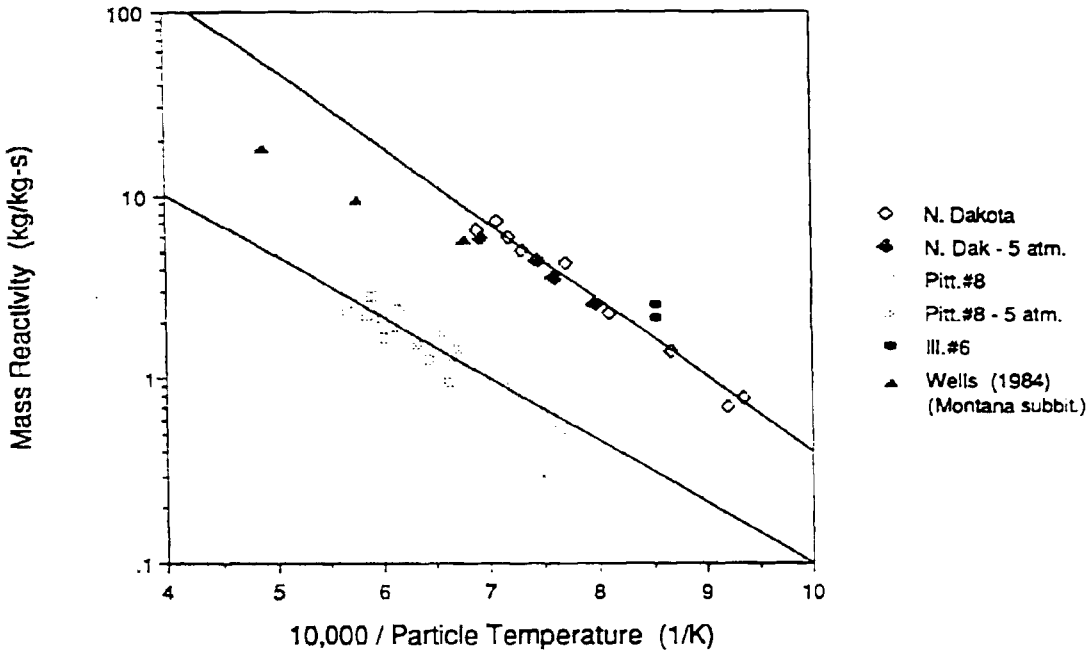

Figure II.B-10. Mass reactivity by ash tracer.

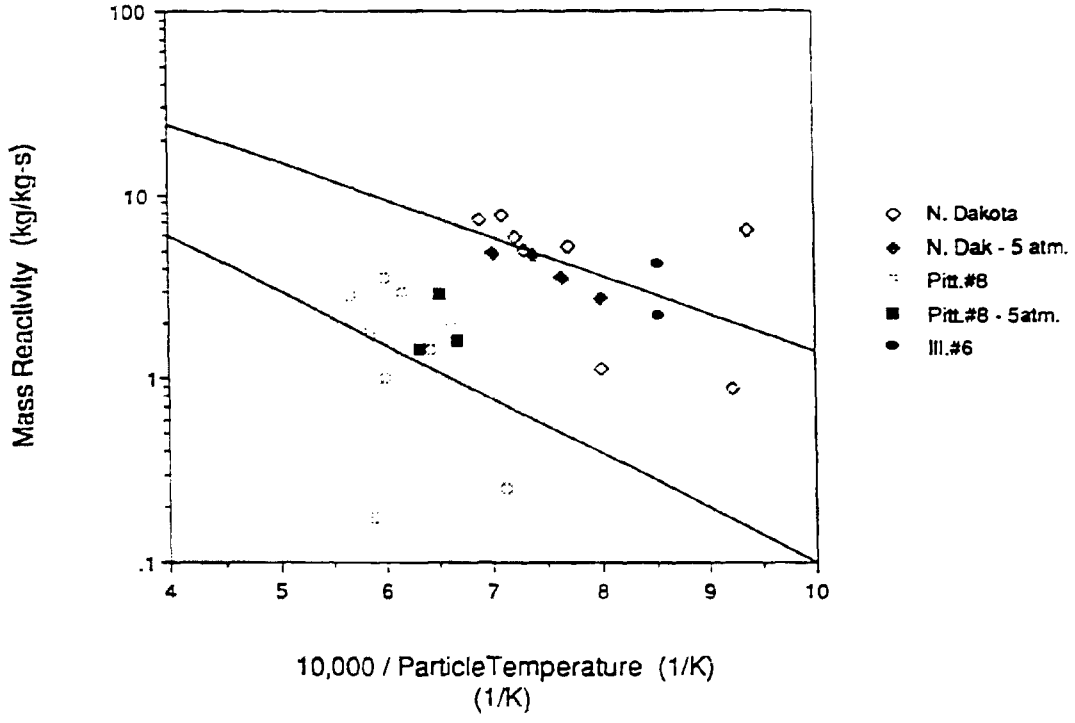

Figure II.B-11. Mass reactivity by titanium tracer.

lies lower by an order of magnitude than the best fit through the other reactivities. This could be a result of the larger particle size or different porosity of the Pittsburgh #8 char. The best fit through the North Dakota char data has a slightly greater slope, indicating a higher activation energy. Reactivities of both Pittsburgh #8 and North Dakota chars oxidized at 5 atm pressure do not appear to be significantly different from their respective atmospheric pressure reactivities. For reference, the activtion energy of the Wells (1984) char was determined to be 31 kcal/mol.

For comparison, an updated plot of mass reactivity vs. particle temperature using titanium as a tracer is shown in Figure II.B-11. The best fit line through the North Dakota char reactivity data corresponds quite closely to data from Wells et al. (1984). However, much more scatter is found in the titanium reactivity data than in the more precise ash reactivity data. It is believed that, for these data, the ash reactivities may be more accurate. The titanium content of a sample was measured using an inductively coupled plasma (ICP) in a manner similar to other researchers who have achieved acceptable accuracy. Efforts continue to improve the accuracy and precision of this crucial analytical process. It appears that an improved sample preparation technique, frequent calibration of the ICP, and multiple measurements of each sample, may be necessary to improve the analysis.

Other Activities

The principal investigators participated in two large review meetings pertaining to this study during the reporting period. A technical review meeting with AFR was held at BYU during March 1990 in which a presentation of results of the project was made to representatives from METC and AFR/BYU. A presentation of the related, but independent, project concerning matched tar/char/gas sets was made at the ACERC annual review meeting, also held in March 1990. ACERC technical associates and affiliates were in attendance at the session, from which helpful suggestions pertaining to this project were received.

Plans

Mounting hardware for the particle imaging system components will be fabricated and the system will be assembled and aligned during the next reporting period. Use of this instrument will greatly improve the accuracy of particle temperature histories. Computer control of the reactor wall heaters

will also be implemented. This will reduce temperature deviation and improve repeatability of reactor conditions in addition to improving ease of reactor operation. During the upcoming quarter the design of the new collection probe and virtual impactor will be completed, built and tested in preparation for coal devolatilization and char oxidation tests. Work will continue to carefully size coal particles prior to char preparation and oxidation. An experimental plan will be finalized for the remaining coals using a predictive reaction code to suggest test conditions.

II.C. SUBTASK 2.c. - SECONDARY REACTION OF PYROLYSIS PRODUCTS AND CHAR BURNOUT SUBMODEL DEVELOPMENT AND EVALUATION

Senior Investigator - James R. Markham and Michael A. Serio
Advanced Fuel Research, Inc.
87 Church Street, East Hartford, CT 06108
(203) 528-9806

Objective

The objective of this subtask is to develop and evaluate by comparison with laboratory experiments, an integrated and compatible submodel to describe the secondary reactions of volatile pyrolysis products and char burnout during coal conversion processes. Experiments on tar cracking, soot formation, tar/gas reactions, char burnout, and ignition will continue during Phase II to allow validation of submodels in Phase II.

Accomplishments

Additional work was done on the coal flame experiments in the TWR using the FT-IR Emission/Transmission Tomography technique. It has been found that the preheated air velocity has a significant effect on the shape of the flame. At low velocities, the ignition point of the flame has a donut-shaped ring of ignition with a cooler center. At high velocities, there appears to be a solid ball of ignited particles. Two cases are being done for the Montana Rosebud coal (low velocity and high velocity) and a low velocity case for the Pittsburgh Seam coal is also being done. The three flames showed both coal and flow dependent phenomena. The slow flow cases showed reduced mixing (more soot and more variations in flame properties with radius) compared to the fast flow case. The Pittsburgh Seam coal showed higher soot, higher swelling, lower particle temperatures, lower char reactivity, and higher volatility compared to the Rosebud coal.

A paper based on this work was accepted for presentation at the 23rd International Symposium of the Combustion Institute.

FT-IR Emission/Transmission Tomography of Coal Flames

Introduction

Fourier Transform Infrared (FT-IR) Emission/Transmission (E/T) spectroscopy has recently been shown to be a versatile technique for coal combustion diagnostics by allowing for measurements of particle concentrations and temperatures, and gas compositions, concentrations, and temperatures (Solomon et al., 1988b). These measurements are for the ensemble of particles and gases along a line-of-sight in the flame.

To correct this shortcoming of the line-of-sight measurements, tomography techniques have been applied to both the FT-IR emission and transmission spectra to obtain spatially resolved spectra from which local flame properties can be obtained. This method has been applied to a stable, well defined co-annular laminar ethylene diffusion flame (Chien et al., 1988; Best et al., 1989). From the spatially resolved spectra, point values for species temperature and relative concentrations were determined for CO_2, H_2O, alkanes, alkenes, alkynes, and soot. Temperatures (for CO_2 and H_2O), and soot concentrations were found to be in good agreement with measurements performed on the same flame by coherent-anti-stokes Raman spectroscopy (CARS) (Boedeker et al., 1986) and laser scattering (Santoro et al., 1983), respectively.

The technique was recently applied to a coal flame produced in a transparent wall reactor (TWR) using a Rosebud subbituminous coal (Markham et al., 1990). From these spectra, spatially resolved point values have been obtained for particle and CO_2 temperatures, relative particle, soot and CO_2 concentrations, the fraction of ignited particles, and the relative radiance intensity.

To study the effect of these conditions on coal type, two more flames have now been characterized. These are a second Rosebud subbituminous coal flame produced using a slower flow of preheated gas and a flame using Pittsburgh Seam coal produced under the same (slow flow) conditions.

Experimental

The TWR facility has been described previously (Solomon et al., 1988b; Markham et al., 1990). The coal is injected upwards into the center of a 10 cm diameter upward flowing preheated air stream in the center of a 20 cm diameter x 70 cm tall glass enclosure. A flow of room temperature air along the perimeter of the reactor keeps the enclosure cool. Radial thermocouple measurements show that the preheated air stream provides a stable hot environment for the coal up to a height of about 30 cm. Our coal feeding system uses a carrier gas which exits the feeder through a tube as it is slowly lowered through a bed of coal particles. Mechanical vibration helps to displace and entrain particles into the tube. A steady feed results in a flame that is stable in shape and position except for the ignition point, where rapid verticle fluctuations of $\pm$ 5 mm are observed. The gas flows used for the high flow case were 2.9 l/sec in the preheated gas and 4.2 x 10^{-3} l/sec in the carrier gas. The gas flows used for the low flow case were 1.7 l/sec in the preheated gas and 3.6 x 10^{-3} l/sec in the carrier gas. The coal feed rate was 0.91 g/min for both cases.

The enclosure has movable KBr windows to allow access to the flame by the FT-IR spectrometer (a modified Nicolet 20SX). As discussed in Best et al. (1986), emission measurements are made by directing the radiation emitted by the hot sample stream through an interferometer to an "emission" detector. Transmission measurements are made by replacing this detector with a high intensity globar source which, after passing through the interferometer, is directed through the sample area to a "transmission" detector. The emission and transmission measurements are made along the same 1 mm wide by 4 mm high optical path defined with apertures. With this optical geometry, twenty-one parallel line-of-sight emission and transmission spectra were collected across the coal stream at 1 mm increments along the radius for each slice. Several slices were obtained for each flame. The spatially resolved "point" values correspond to an average within 1 mm x 1 mm x 4 mm high volumes. In this work the data were smoothed by co-adding data from eight adjacent wavenumber bands. This results in degraded resolution from the 8 cm^{-1} used, although still sufficient to quantitatively measure the gas species.

The samples used in this experiment were sieved fractions (200 x 325 mesh) of dry Montana Rosebud subbituminous coal and dry Pittsburgh Seam coal. The characteristics of these coals have been published previously (Solomon et al., 1988b; Serio et al., 1987).

Analysis

The analysis for the line-of-sight FT-IR E/T measurement pertaining to multi-phase reacting streams has been presented previously (Solomon et al., 1988b; Markham et al., 1990; Best et al., 1986; Solomon et al., 1987a,b,c). The relative concentrations and temperatures for individual components (gas, soot, and particles) are obtained from the transmission and normalized radiance spectra, respectively, as discussed in Solomon et al. (1988b), Markham et al., (1990), Best et al. (1986), and Solomon et al. (1987a,b,c).

The reconstruction of spatially resolved FT-IR spectra from multiple line-of-sight spectra was first introduced elsewhere (Chien et al., 1988; Best et al., 1989; Markham et al., 1990). We have employed the standard Fourier image reconstruction technique (Shepp and Logan, 1974) which is capable of handling data from systems of arbitrary shape. Our flame, however, was cylindrically symmetric. The computer program published by Shepp and Logan was used for this work (Shepp and Logan, 1974) by applying the reconstruction one wavelength at a time to determine spatially resolved spectra.

A straight-forward application of the reconstruction technique to radiance spectra is not possible, because of self-absorption in the sample. In the case of small absorbance encountered in this work (percent transmission > 80%), an emission measurement can be directly corrected by an absorption measurement made along the same path. A self-absorption correction corresponding to that used by Freeman and Katz (1960) was employed for the thin sample studied. The Fourier reconstruction program can be applied directly to the emission thus corrected, to obtain local radiances. These are then converted to normalized radiance and the analysis proceeds as for the line-of-sight spectra.

Results

Flame Characteristics - The three flames are presented in Fig. II.C-1. All three flames are characterized by a bright ignition zone followed by a region of lower intensity where burnout is occurring. Photographs show the high intensity zone to contain burning volatile clouds which are 3 to 5 times the diameter of the particles. The Pittsburgh Seam coal shows a region of distinct dimness after ignition which may occur after the initial oxygen is consumed by the volatiles.

Measurements were made of the particle velocities by measuring the length of tracks recorded with a video camera using a 1/250 shutter speed. The results are presented in Fig. II.C-2. The particles accelerate as they leave the nozzle due to the heating of the carrier gas, the influence of the faster hot gas surrounding the carrier gas stream, and buoyancy effects. At ignition, the acceleration is increased as the center stream is rapidly heated. The data show the velocities increasing to above the hot gas velocity. The heating of the central stream appears to dominate the particle velocity as the two cases where the hot gas velocity is lowest (Fig. II.C-2b and II.C-2c) produce a higher particle velocity than in Fig. II.C-2a where the hot gas velocity is higher. Based on these velocities, the particle residence times (given in Fig. II.C-1) were computed.

The tomography data for these three flames are presented in Figs. II.C-3 to II.C-5. The seven parameters which were measured are: a) relative particle and soot concentrations, b) the multiplier M which is the emissivity times the fraction of particles at the measured temperature, c) the spectral radiance at 4500 cm^{-1}, d) the particle and CO_2 temperatures, and e) the CO_2 concentration.

The tomography data for the Rosebud fast flow case are presented in Fig. II.C-3. These data were presented previously (Markham et al., 1990) but are reproduced here for comparison. Figure II.C-3a presents the height of the continuum blockage determined from the transmittance spectra as percent blockage of the incident IR beam. The blockage is divided into particles and soot. Soot is observed to appear at ignition, as inferred by the change in shape of the continuum as described below. Below the ignition point (6 cm above the 4 mm

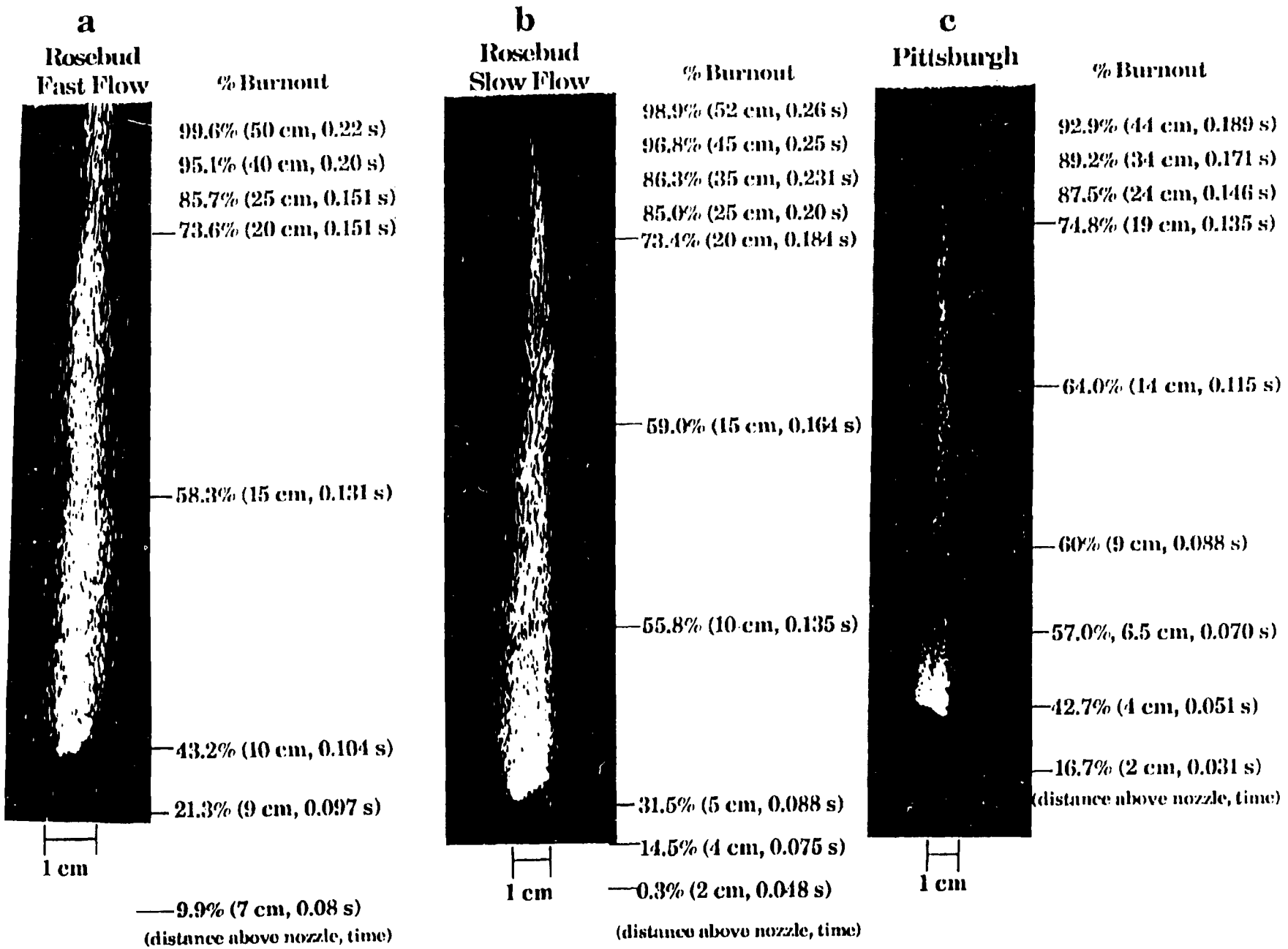

Figure II.C-1. Photographs of Coal Flames in the TWR. a) Rosebud Subbituminous - Fast Flow, b) Rosebud Subbituminous Coal - Slow Flow, and c) Pittsburgh Seam Bituminous - Slow Flow. % Burnout as Determined from Particle Collections in each Flame is Indicated.

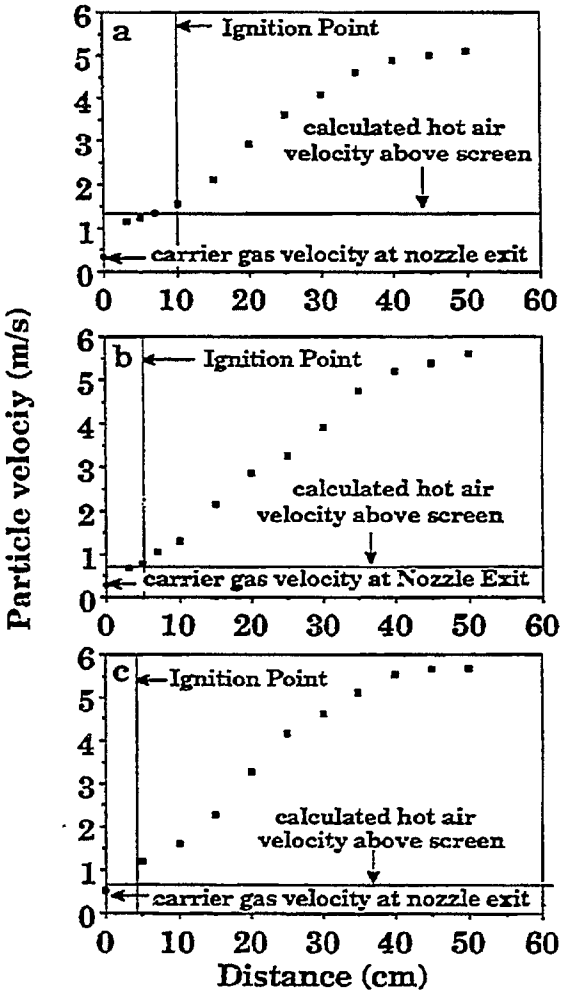

Figure ILC-2. Particle Velocities as a Function of the Distance Above the Nozzle. a) Rosebud Subbituminous Coal - Fast Flow, b) Rosebud Subbituminous Coal - Slow Flow, and c) Pittsburgh Seam Bituminous Coal - Slow Flow.

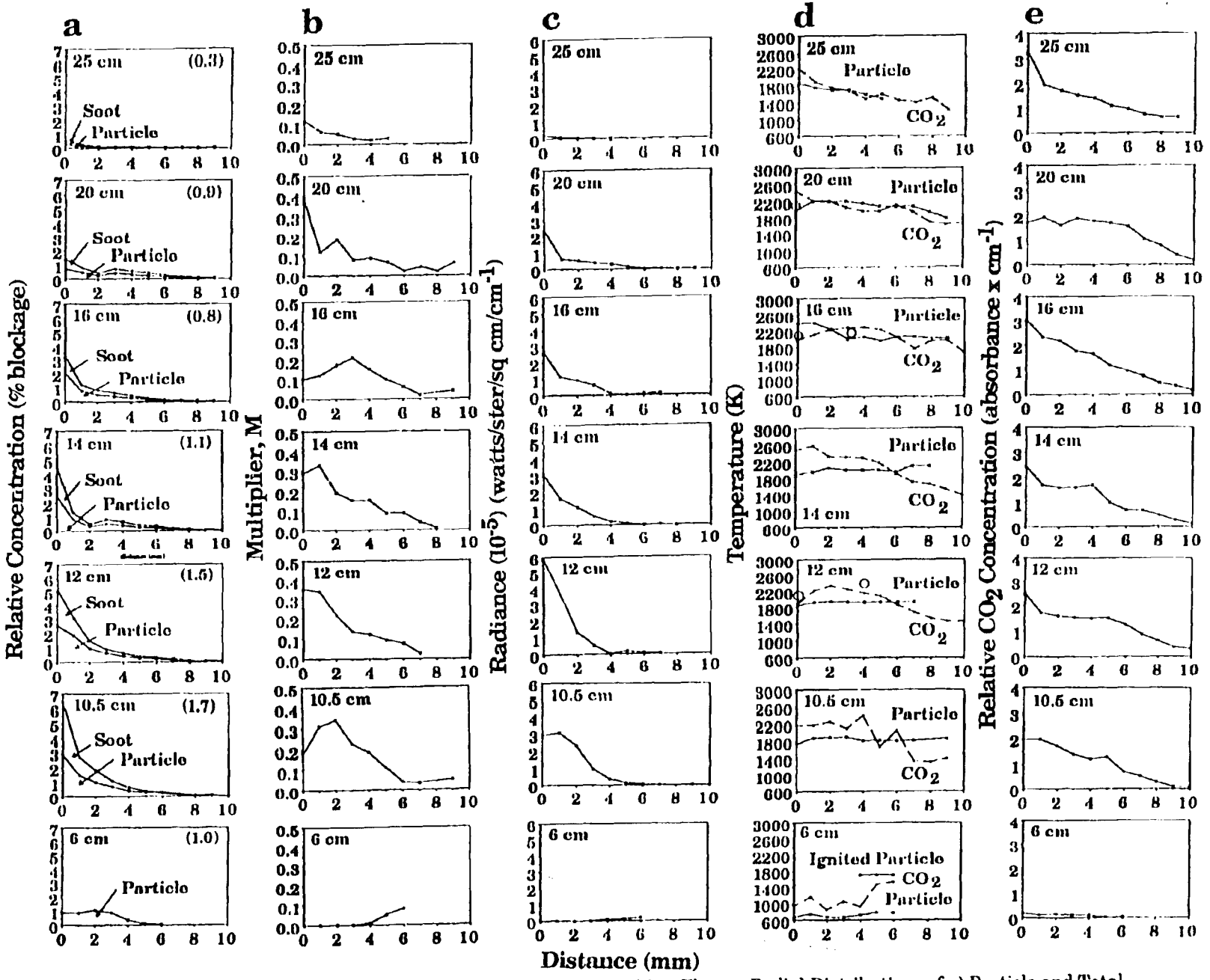

Figure II.C-3. Data for Rosebud Subbituminous Coal - Fast Flow Flame. Radial Distributions of a) Particle and Total (particle + soot) Concentration. Integrated Particle Blockage is Indicated in Parenthesis; b) Multiplier for IgnitedParticles (Black-body intensity); c) Spectral Radiance at 4500 cm^{-1}; d) Particle (solid) and CO_2 (dashed) Temperature; e) CO_2 Concentration at Indicated Distances above the Nozzle for a Rosebud Coal Flame in the TWR.

diameter nozzle) there are particles only (no soot) confined to a radius of about 6 mm. This is in agreement with the boundaries as determined by scattering of a He-Ne laser beam. The multiplier, M (the product of emissivity times the fraction of ignited particles in Fig. II.C-3b shows a few particles (up to 10%) have ignited at the edge of the coal stream. Such ignited particles can also be seen in Figs. II.C-1b and II.C-1c.

Just above ignition (10.5 cm above the nozzle), the particles appear to be forced inward into a more dense central stream at the same time that some particles are spread outward. The spreading of the stream is confirmed visually. This spreading is consistent with the location of the ignition zone centered at about 2 mm radius, indicated by the 0.35 M value in Fig. II.C-3b (i.e., approximately one-third of the particles ignite). Considerably less material is ignited at the center and outer region of the ignition zone. The increase in gas volume in this zone acts to compress the stream inward and expand the stream outward. The total particle blockage (number in parentheses in Fig. II.C-3a) determined by integrating the blockage times area indicates that the blockage is increased from 1.0 (by definition) at 6 cm to 1.7 at 10.5 cm to 1.5 at 12 cm. This suggests that the devolatilization, which appears complete at this point, may swell or fragment the particles to increase the blockage. Swelling is observed in SEM photographs of collected particles. Above 12 cm, the particle blockage is reduced as the material burns out (Fig. II.C-3a).

The multiplier, M (Fig. II.C-3b), indicates that the ignition zone quickly collapses to the center axis (compare 10.5, 12, and 14 cm). From 14 cm through 16 cm, M again drops near the center region, but this may be caused by a build-up of ash in the center region, as evidenced by a corresponding drop in the relative amount of soot compared to particles at these positions. At 20 cm, an increase in blockage at radiuses above 4 mm is observed (ash dispersion) with a corresponding decrease in M above 4 mm and an increase in M at the center.

Figure II.C-3c presents the local radiance determined at 4500 cm^{-1}. At 6 cm, high frequency radiance is detected from the previously mentioned few particles that are observed to ignite at the edge of the coal stream. Just above the ignition point (10.5 cm), the high values of radiance along the center result from the high density of particles blockage, even though M may be low.

The radiance from 10.5 cm to 12 cm is observed to increase along the center, as was observed for M.

Figure II.C-3d presents the temperature of CO_2 (dashed line) and total continuum, both particles and soot (solid line). Also presented are measurements with a Pt + Pt/Rh thermocouple obtained in the flame at the 12, 16, and 20 cm positions. The particles have a relatively constant temperature between 1800 and 1900 K at 10.5 and 12 cm. The cooler center region at 10.5 cm (in agreement with M and radiance) is observed. Particle temperature increases from 1900 K to 2000 K at 14 cm, and to 2200 K to 2400 K through 16 to 20 cm. Above 20 cm, the temperature falls.

The maximum CO_2 temperatures (2200 to 2600 K) occur in the regions of high particle radiance where the maximum combustion is occurring, although the center temperatures at 12 and 16 cm are puzzling. In the beginning region of the flame, CO_2 is 400 to 700 K hotter than the particles in the same region suggesting that CO is burning to CO_2 away from the particles. CO_2 temperatures are generally closer to the particle temperatures above 14 cm. At the edge of the stream the CO_2 temperature is always lower due to rapid heat transfer to the surrounding air. At 20 cm, the CO_2 and particle temperatures are within 100 K except along the axis where the CO_2 is hotter.

The CO_2 concentrations are presented in Fig. II.C-3e. Below ignition, the CO_2 concentration is very small. Above ignition, the CO_2 level jumps drastically and spreads with increasing height. These data present a picture of the coal burning in a shrinking region which collapses to the center at the tip of the flame.

The results for the two other flames are presented in Figs. II.C-4 and II.C-5. The trends are qualitatively similar. There are, however, differences in the soot formation, swelling, ignition, particle temperatures, burnout, and CO_2 concentrations, and these will be discussed below.

Soot Formation - As described previously (Solomon et al., 1988b) the shape of the continuum spectra can be employed to separate the contributions from particles and soot. Two spectra for the Pittsburgh Seam coal are presented

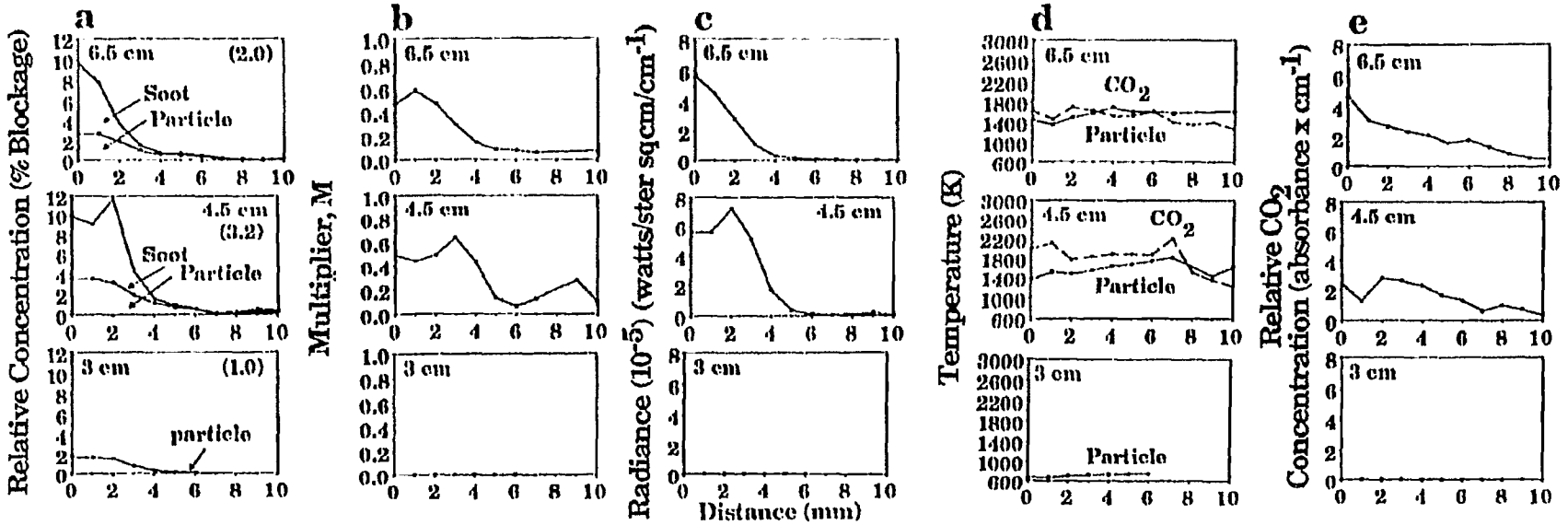

Figure II.C-4. Data for Rosebud Subbituminous Coal - Slow Flow Flame. Radial Distributions of a) Particle and Total (particle + soot) Concentration. Integrated Particle Blockage is Indicated in Parenthesis; b) Multiplier for IgnitedParticles (Black-body intensity); c) Spectral Radiance at 4500 cm^{-1}; d) Particle (solid) and CO_2 (dashed) Temperature; e) CO_2 Concentration at Indicated Distances above the Nozzle for a Rosebud Coal Flame in the TWR.

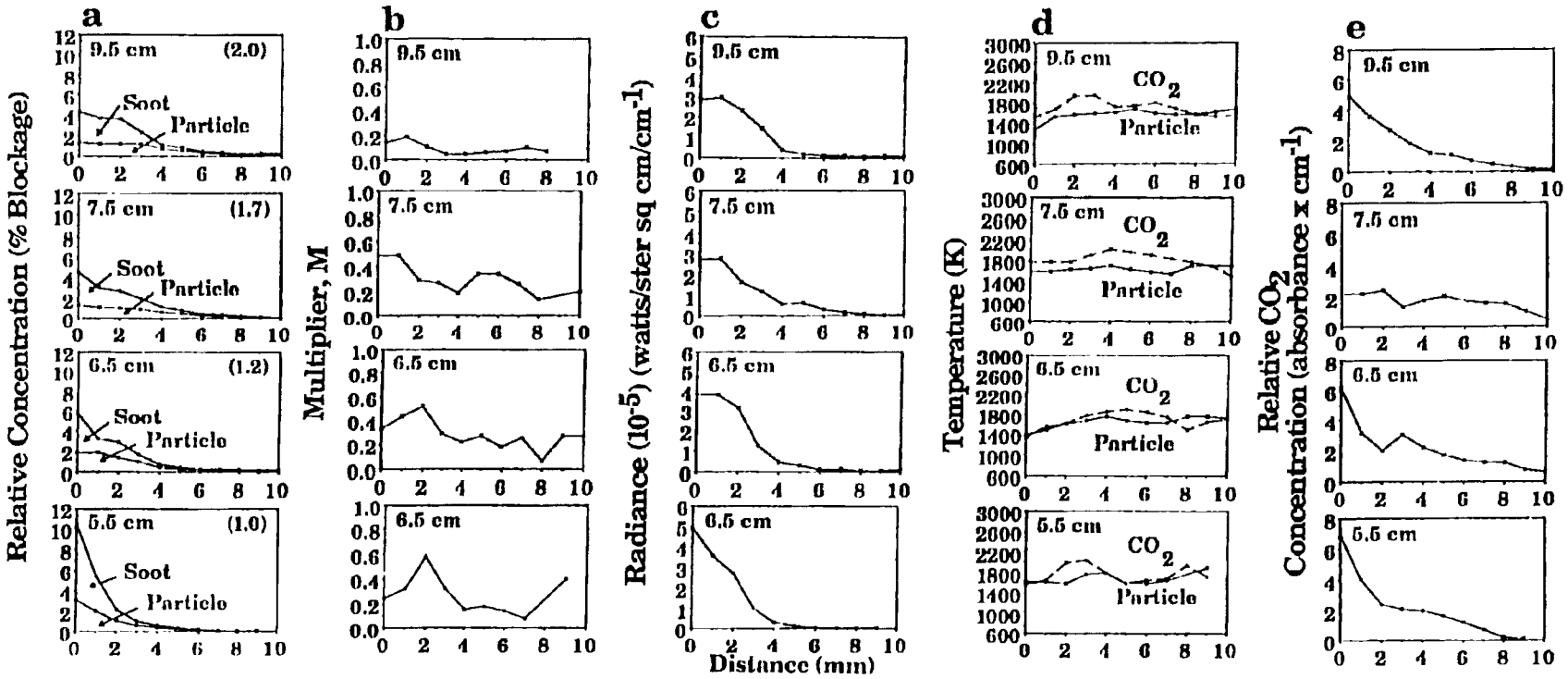

Figure II.C-5. Data for Pittsburgh Seam Bituminous Coal - Slow Flow Flame. Radial Distributions of a) Particle and Total (particle + soot) Concentration. Integrated Particle Blockage is Indicated in Parenthesis; b) Multiplier for Ignited Particles (Black-body intensity); c) Spectral Radiance at 4500 cm^{-1}; d) Particle (solid) and CO_2 (dashed) Temperature; e) CO_2 Concentration at Indicated Distances above the Nozzle for a Rosebud Coal Flame in the TWR.

in Fig. II.C-6. Figure II.C-6a presents 1-τ, where τ is the transmittance, prior to ignition where no soot is present. The upward slope toward low wavenumbers (long wavelengths) is due to diffraction. Figure II.C-6b presents a spectrum above ignition in the region of high soot. The spectrum now slopes in the opposite direction due to soot. To resolve the spectrum into particle and soot contributions, the frequency dependent extinction efficiency, F'_ν, for the particles (which is proportional to (1-τ)) is assumed to have the same shape as prior to ignition, and the particle transmittance is assumed to be equal to the measured transmittance extrapolated to 0 cm^{-1} (where the attenuation from soot goes to zero). A straight line extrapolation is made below 3500 cm^{-1} excluding the region of the spectrum containing CO_2 and H_2O bands. The soot contribution is the difference between the particle attenuation and the total, as shown in Fig. II.C-6c.

The relative amounts of soot can be seen in Figs. II.C-3a, II.C-4a, and II.C-5a. The soot concentration is highest just above ignition. The highest soot concentrations are observed for the Pittsburgh Seam coal followed by the Rosebud slow case and then the Rosebud fast case. For Pittsburgh Seam, the highest attenuation from soot is about three times that from the particles. For Rosebud (slow flow) the highest value is only 2.3 times and for Rosebud (fast flow) only a little over 1 times. The variation in soot concentration comes from two factors: 1) tar, which is the soot precursor (Solomon et al., 1988b) is higher for Pittsburgh Seam coal than for Rosebud, and 2) the better mixing in the fast flow increases the oxygen to the central core which reduces the soot.

Swelling and Fragmentation - The swelling or fragmentation of the particles is indicated by the integrated particle blockage values as a function of position. The 6 cm case of the Rosebud and the 4 cm case for the Pittsburgh provide the baseline before ignition. Both cases show a flat distribution over the center 2 mm which goes to zero between 4 and 5 mm. The integrated blockage is given in parenthesis on each of the figures.

If there was no swelling or fragmentation, the blockage would decrease due to the gas heating. For the Pittsburgh Seam coal, the integrated blockage more than triples. Photomicrographs of samples collected in the flame show both

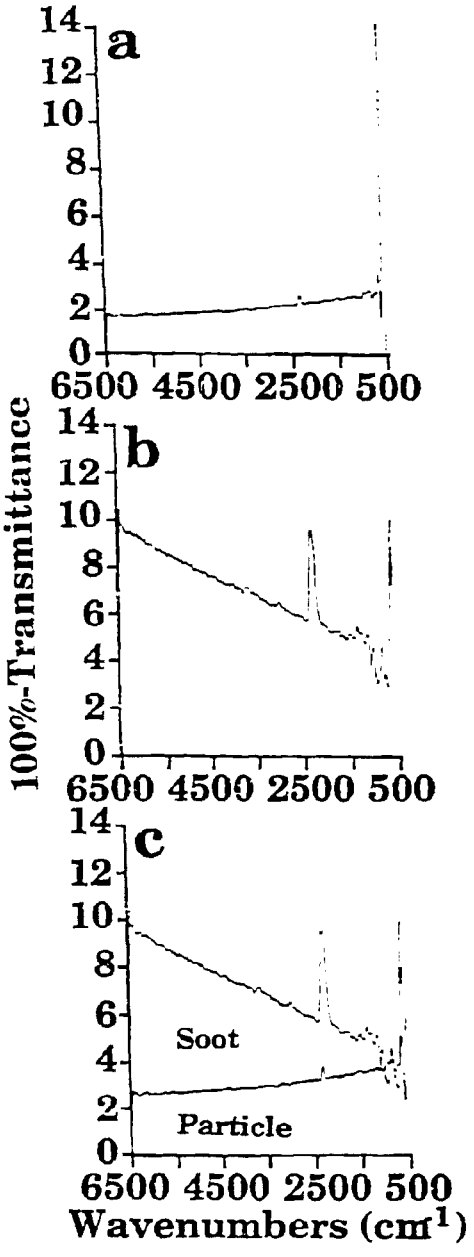

Figure II.C-6. Analysis to Resolve Continuum Blockage Spectrum into Particle and Soot Contributions. a) Particle Blockage Below Ignition, b) Total Particle and Soot Blockage above Ignition, and c) Contribution of Each Component to Total Blockage.

swelling of coal and the appearance of small ash particles. Both changes would increase the blockage. For the Rosebud coal, the increases are more modest. While swelling was observed for the fast flow case, the slow flow case does not indicate an obvious swelling or rounding.

Ignition - Ignition for all three cases occurs with the outside of the particle stream (which is in best contact with the hot gases) igniting first. This can be seen in the multiplier M, which is the fraction of ignited particles, in Figs. II.C-3b, II.C-4b, and II.C-5b. At ignition, M is highest at the edge of the particle stream. A photograph in Fig. II.C-7 looking at the ignition zone of the Rosebud slow case clearly shows the ring of ignition. The Pittsburgh, which is also a slow flow case, exhibits a similar ring while the faster flow case, which appears to have better mixing, shows the same effect but to a lesser degree. Ignition at the edges is consistent with the particle temperatures below ignition (Fig. II.C-5d) which indicate that the particles at the edge of the stream have reached 800 K while those in the center are as low as 600 K.

Temperatures - The following observations can be made about particle temperatures. 1) Particle temperatures are highest at the edge of the flame where the concentration of oxygen is highest. 2) The lowest temperatures are observed for the Pittsburgh Seam coal, while the highest temperatures are observed for the fast flow Rosebud case. Particle temperatures are generally in the range 1400 to 2200 K.

CO_2 temperatures are always higher than the particle temperatures in the combustion region suggesting that most CO_2 is produced away from the particle surface (e.g., by CO oxidation). The highest CO_2 temperatures were observed in the fast flow case and approached 2600 K.

Burnout - The percent weight loss as a function of distance above the nozzle for the three flames is indicated in Fig. II.C-1, and plotted in Fig. II.C-8. Both slow flow cases display a transient plateau in their burnout profiles which begin within 5 cm past their respective ignition points. Rapid oxygen consumption and inadequate mixing of the surrounding air is believed to cause this effect, which is not displayed for the fast flow (better mixing) case. Both Rosebud flames exhibit essentially 100% DAF burnout by 50 cm above

Figure II.C-7. Photograph of Rosebud Subbituminous Coal - Slow Flow Flame Taken from Above the Ignition Region.

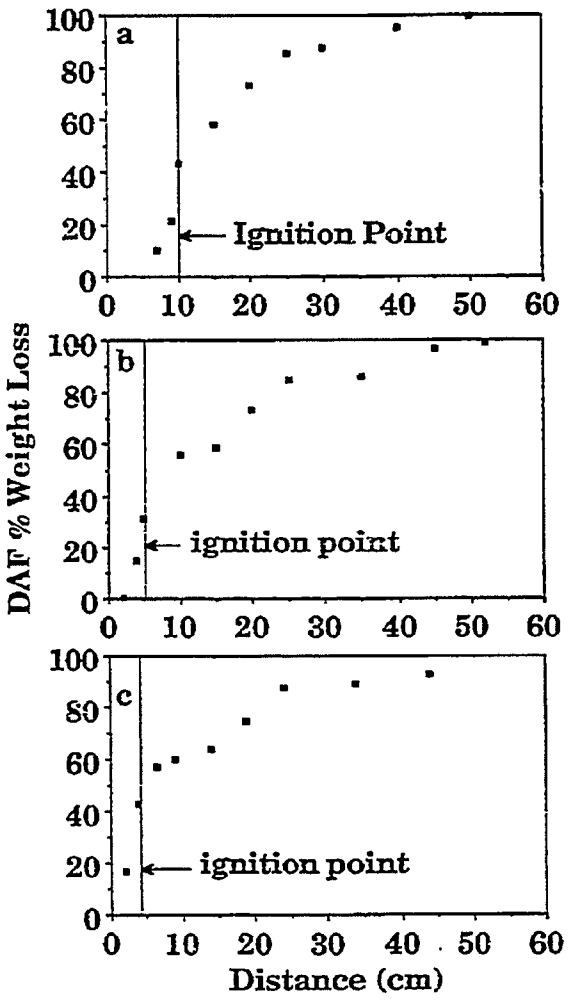

Figure II.C-8. DAF % Weight Loss (burnout) as a Function of Distance Above the Nozzle for a) Rosebud Coal - Fast Fl , b) Rosebud Coal - Slow Flow and c) Pittsburgh Coal - Slow Flow.

the nozzle. The Pittsburgh flame, however, seems to contain - 10% char which displays a very low reactivity.

CO_2 Concentration - The concentration of CO_2 for all cases generally decreased with distance away from the centerline for each slice. The slow flow Rosebud case showed an overall larger amount of CO_2 in the combustion region than the fast flow Rosebud case, but this may be attributed to less mixing (and hence, less dilution) for the slow flow condition.

Conclusions

Tomographic reconstruction techniques have been applied to FT-IR E/T measurements to derive local values for species temperatures and concentrations within three laboratory scale coal flames. Values for particle temperature, relative particle density, relative soot concentration, the radiance intensity, the relative CO_2 concentration and the CO_2 temperature have been obtained as functions of distance from the flame axis and height above the coal injector nozzle. The spectroscopic data are in good agreement with visual observations and thermocouple measurements. These data present a picture of the coal burning in a shrinking region which collapses to the center at the tip of the flame. CO_2 temperatures are highest in the rapid burning zone (2200 to 2600 K). The highest particle temperatures in this zone are 1900 to 2000 K, with temperatures up to 2400 K outside the zone. The three flames showed both coal and flow dependent phenomena. The slow flow cases showed reduced mixing (more soot and more variations in flame properties with radius) compared to the fast flow case. The Pittsburgh Seam coal showed higher soot, higher swelling, lower particle temperatures, and lower char reactivity compared to the Rosebud coal.

Plans

Complete tomography measurements for the two different coals (Montana Rosebud subbituminous, Pittsburgh Seam bituminous). Do color maps for presentation of tomography data. Continue characterization of TWR geometry and interact with BYU on PCGC-2 simulations of this system.

II.D. SUBTASK 2.d. - ASH PHYSICS AND CHEMISTRY SUBMODEL

Senior Investigators - James Markham and Michael Serio
Advanced Fuel Research, Inc.
87 Church Street, East Hartford, CT 06108
(203) 528-9806

Objective

The objective of this task is to develop and validate, by comparison with laboratory experiments, an integrated and compatible submodel to describe the ash physics and chemistry during coal conversion processes. AFR will provide the submodel to BYU together with assistance for its implementation into the BYU PCGC-2 comprehensive code.

To accomplish the overall objective, the following specific objectives are: 1) to develop an understanding of the mineral matter phase transformations during ashing and slagging in coal conversion; 2) To investigate the catalytic effect of mineral matter on coal conversion processes. Data acquisition will be focused on: 1) design and implementation of an ash sample collection system; 2) developing methods for mineral characterization in ash particles; 3) developing methods for studying the catalytic effects of minerals on coal gasification.

Accomplishments

Work began on characterizing the reactivity of chars collected from the coal flame experiments. These chars have been analyzed by the standard TG-FTIR analysis which directly provides information on the reactivity index ($T_{critical}$) and the active site concentration (based on the amount of oxygen chemisorbed). A correlation was found between these two measurements, which was expected since the theory on which $T_{critical}$ is based relates it to the inverse of the product of the active site concentration and the accessible surface area. In order to apply this technique to the high ash chars from the coal flame, a method was developed to correct the $T_{critical}$ for the char ash content. This is described in Appendix A. Our next step is to do Temperature Programmed Desorption (TPD)

measurements on these chars, which will provide additional information on the reactivity and the distribution of active sites.

Plans

Continue study of mineral effects on the reactivity of low and high rank coals. Resume analysis of material and element balances from ash collections in the entrained flow reactor.

II.E. SUBTASK 2.e. - LARGE PARTICLE SUBMODELS

Senior Investigator - Michael A. Serio
Advanced Fuel Research, Inc.
87 Church Street
East Hartford, CT 06108
(203) 528-9806

Objective

The objectives of this task are to develop or adapt advanced physics and chemistry submodels for the reactions of "large" coal particles (i.e., particles with significant heat and/or mass transport limitations) and to validate the submodels by comparison with laboratory scale experiments. The result will be coal chemistry and physics submodels which can be integrated into the fixed-bed (or moving-bed) gasifier code to be developed by BYU in Subtask 3.b. Consequently, this task will be closely coordinated with Subtask 3.b.

Accomplishments

The experimental work on the AFR fixed-bed reactor (FBR) system continued with the Pittsburgh Seam bituminous and Zap lignite coals. For both coals, we have not observed a strong effect of bed depth on tar yield over the range of conditions studied. For the Pittsburgh coal, there was some effect on tar composition, with the deeper beds giving tars which were more aliphatic (less aromatic). A second series of pyrolysis experiments was done with the FBR using Pittsburgh Seam bituminous coal. The reactor was modified so that the coal could be held in two separate layers on top of each other with a gap in between. The experiments were done at two different flow rates. The higher flow rate resulted in an increase in tar and a decrease in CH_4 and char yields in both the single and dual bed experiments. The two layer configuration, with about a 150°C temperature difference between them, resulted in a large increase in methane yields at low flow rates and a small decrease in the tar yield at high flow rates.

Discussions were held with BYU about the single particle FG-DVC model. Work was completed on a percolation theory version which is based on a system of ordinary differential equations which describes the creation and loss of n-oligomers. This version will be the basis for the single particle FG-DVC model which will be input into the fixed bed code being developed at BYU. Our current tests indicate that this version is somewhat slower than the original version. Work is currently being done to make it more efficient.

Fixed-Bed Reactor Experiments

The work on the AFR fixed-bed reactor (FBR) system continued. Several experiments were done with Pittsburgh Seam bituminous coal which covered a range of bed depths. There did not appear to be a strong effect of bed depth on tar yield over the range of conditions studied. There was some effect on the tar composition, with the deeper beds giving tars which were more aliphatic (less aromatic).

There did appear to be some very interesting effects on the temperature of the maximum tar evolution rate as bed depth increased. Initially, this value remained fairly constant, then went up dramatically. This increase coincided with the evolution of the tar by a "bursting" phenomenon in the bed rather than from individual particles. One problem with the tar "burst" is that it interferes with the quantitation of the gases during that period. Consequently, we are planning to redesign the system so that we can separate most of the tar prior to the gas cell.

Additional experiments were done with Zap lignite coal. In the case of the Zap, there were no problems in gas quantitation due to a "tar burst" which happened from the Pittsburgh Seam coal due to the significantly larger tar production. The tar amounts from the fixed bed experiments with the Zap lignite coal for small amounts of coal agree fairly well with the TG-FTIR results. As the bed depth increased, the tar yield was the same within the reproducibility of the measurements.

A second series of pyrolysis experiments was done with the fixed-bed reactor using Pittsburgh Seam bituminous coal. The reactor was modified so that the coal could be held in two separate layers on top of each other with a gap in between. The temperatures of the sweep gas and of the top coal layer were continuously monitored during the experiment. The temperature of the lower layer was approximately 100-200°C less than the upper layer depending on the flow rate and the gas temperature. The objective of these experiments was to measure the occurrence of tar recondensation on the lower layer. A glass wool tar filter was used to make quantitative measurements of tar yields. When the tar filter was in place, lower yields of gases were obtained and the T_{max} values came at higher temperatures. This could be attributed to either gas adsorption on the tar filter or on the tar particles.

Since the maximum temperature that could be reached in the top layer (I) was ~ 600°C, the second layer (II) could not reach high enough temperatures for all of the tar to be volatilized. Therefore, a second run was done with the char from layer II placed in layer I. A key to the various reactor configurations is given in Table II.E-1. Three different configurations of the reactor system were used. Setup A was used to obtain the baseline tar yield from the first layer. Setup B was the experiment to measure the effect of having a lower temperature coal layer in series. Setup C was used to obtain the baseline tar yield from the second layer.

The experiments were done at two different flow rates. The detailed results are given in Table II.E-2. The FBR system provides good reproducibility for the single bed geometry. Duplicate experiments for the dual bed configuration are planned for the next quarter. The preliminary conclusions from these data are as follows:

1) The higher flow rate resulted in an increase in tar and a decrease in CH_4 and char yields in both the single and dual bed experiments.

2) The two layer configuration, with about a 150°C temperature difference between them, resulted in a large increase in methane yields at low flow rates and a small decrease in the

TABLE II.E-1 - CONFIGURATION OF FIXED-BED REACTOR

	FIRST RUN		SECOND RUN	
Setup	Layer I	Layer II	Layer I	Layer II
A	coal	empty	———	———
B	coal	coal	II char	empty
C	char	coal	II char	empty

TABLE II.E-2 - SUMMARY OF EXPERIMENTAL RESULTS FROM EXPERIMENTS WITH TWO BEDS OF PITTSBURGH SEAM COAL IN THE FIXED-BED REACTOR

			FIRST RUN						SECOND RUN					TOTAL		
					Yield Weight %						Yield Weight %					
			T_{max} °C		I + II		Char		T_{max} °C		II		Char	Σ Yield		
Setup	He Flowrate ml/min	Tar Filter	Tar	CH_4	Tar	CH_4	I	II	Tar	CH_4	Tar	CH_4	II	Tar	CH_4	Char
A (I)	400	Yes	530	530	19.1	2.6	67.0							19.1	2.6	67.4
		No	457	486			67.8									
B (I+II)	400	Yes No	474	497	16.8	3.8	70.0	80.7	527	571	7.6	4.6	86.2	19.9	5.7	68.3
C (II)	400	Yes No			15.1	1.0		81.8	538	570	7.7	2.5	84.4	21.3	3.0	69.1
A (I)	1240	Yes No	487	501	26.3	0.8	68.6							26.3	0.8	68.6
B (I+II)	1240	Yes No	560	505	16.6	0.1	66.4	85.1	471	520	12.3	2.0	79.1	23.0	1.0	66.8
C (II)	1240	Yes No			*7.5	0.1		84.5	492	535	9.8	1.9	81.0	16.0*	1.6	68.4

* May be exp. error

tar yield at high flow rates.

3) In a separate set of experiments, the pyrolysis was stopped at different temperatures to measure the weight of the first (I) and second (II) layer chars. The results show that a weight gain occurred for the II layer at ~ 300°C (assuming ~ 150°C average temperature difference between the two layers) coincident with the temperature of the maximum tar evolution rate from the first layer.

4) It appears that most of the tar which is condensed onto the cooler layer can be revolatilized under the conditions that have been studied to date. However, the percentage of tar which does revolatilize and the temperature at which this occurs appear to be sensitive to oxidation.

Single Particle Model

Discussions were held with BYU about the single particle FG-DVC model. Additional details were sent to BYU on the theory of the DVC portion of the model to help them with the integration of the FG-DVC model into the Advanced Fixed Bed Model. Work was completed on a percolation theory version which is based on a system of ordinary differential equations which describes the creation and loss of n-oligomers. The LSODE package is being used for integration. This version will be the basis for the single particle FG-DVC model which will be input into the fixed bed code being developed at BYU. Our current tests indicate that this version is somewhat slower than the original version. Work is currently being done to make it more efficient.

Plans

Complete initial set of experiments on secondary reaction effects in thick beds. Complete redesign of fixed-bed reactor system. Continue development of single particle model with BYU. Begin work on tar repolymerization model.

II.F. SUBTASK 2.F. - LARGE PARTICLE OXIDATION AT HIGH PRESSURES

Senior Investigators: Angus U. Blackham and Geoffrey J. Germane
Brigham Young University
Provo, Utah 84602
(801) 378-2355 and 6536

Student Research Assistants: Gary Pehrson and Michael Scheetz

Objectives

The objective of this subtask is to provide data for reaction rates of large char particles of interest to fixed-bed coal gasification systems operating at pressure.

Accomplishments

Work continued on the design of a large-particle insert to be used in the HPCP reactor being used in Subtask 2.b. The apparatus consists of (a) a reactor tube, (b) a balance unit, and (c) a connecting pipe. A Varian gas chromatograph has been obtained for use in monitoring product gas composition (particularly carbon monoxide and carbon dioxide). A new column has been ordered and will be evaluated next quarter. A preliminary set of large-particle oxidation tests were conducted with Utah bituminous coal char in platinum crucibles. Mass reactivities have been calculated and the results appear to be satisfactory. Additional preliminary experiments will be conducted during the construction of the large-particle insert. These tests will help guide the experimental design.

High-Pressure, Large-Particle Reactor Design

Experimental Approach - Analytical - One of the methods under consideration for monitoring the rates of oxidation of large particles is the gas chromatographic analysis of the gaseous products, particularly CO and CO_2. In addition to following the rate of mass loss, this procedure will also give insight into the mechanism of the reaction by observing the ratio of CO to CO_2. A Varian gas chromatograph will be used for this analysis. In order to measure both CO and CO_2, other experimenters have used two columns with switching valves to include or exclude one of the columns in the carrier gas flow path. Sometimes special cooling facilities have been required

(liquid CO_2 sprayed into the temperature control chamber for the columns). A new approach is available in which one column is used with dual packings to provide more rapid analysis of a sample. This column is being ordered and will be evaluated during this next quarter.

In Subtask 2.b and other on-going projects, the rates of oxidation are being monitored by analyzing the chars for ash content and titanium content. This procedure will also be evaluated for use with large-particle oxidation.

Experimental Reaction Rate Data

Preliminary Large Particle Oxidation Measurements - Preliminary experiments were conducted with char prepared from Utah bituminous coal in platinum crucibles. Six particles with dimensions of approximately 0.5-1.0 cm on a side were prepared from a single lump of coal and individually devolatilized and oxidized Each crucible was placed on a clay wire triangle on its side so air could flow into the crucible and around the coal particle. Each crucible was heated with a Mekker burner so that the flame passed across the mouth of the crucible. As the particle increased in temperature the devolatilization started and the evolved gases were burned in the flame at the mouth of the crucible. This continued for two to three minutes until no further burning of gases was observed. The crucibles were cooled and weighed, then heated again while the char oxidized for five minutes. The samples were cooled and weighed, then heated again for five minutes. The process was repeated a few more times until only ash remained, the period of heating increasing as the burnout increased. The sum of the heating periods was approximately sixty minutes. These data are presented in Table II.F-1 and Figure II.F-1. The masses of the samples ranged from 0.310 to 0.702 grams; the percent volatiles from 42.2 to 49.6%; the ash from 2.85 to 3.87%. The temperature measured by placing a thermocouple into the crucibles was approximately 1150 K. The mass reactivities calculated successively through each run are listed in Table II.F-1. The average value through the entire set with the exclusion of the low values from the last heating period give a mass reactivity of 0.0475 min^{-1} .

A significant observation was that the ash particle remaining at the end of the heating period was about the same shape and size as the starting coal particle. The porosity had increased without significant swelling or shrinking.

TABLE II. F -1

PRELIMINARY LARGE PARTICLE OXIDATION MEASUREMENTS

Coal: Utah Bituminous
Temperature: approximately 1150K
Conditions: Oxidation in Air with Platinum Crucibles and Mekker Burners

Crucible	#1	#2	#3	#4	#5	#6
Mass of Sample (grams)	0.386	0.609	0.662	0.702	0.445	0.310
%Volatiles	48.2	49.6	44.4	47.2	42.2	42.6
% Ash	2.85	3.28	3.47	3.13	2.92	3.87
			Mass Reactivity (Minutes^{-1})			
Time (minutes)						
7.5	.065	.046	.033	.046	.061	.061
12.5	.071	.042	.043	.048	.040	.045
17.5	.085	.036	.036	.027	.046	.058
27.5	.032	.042	.040	.042	.061	.069
42.5	.041	.039	.045	.045	.042	.029
57.5	.010	.031	.026	.026	.013	
Average (except last value)	.0588	.0410	.0405	.0415	.0500	.0524
Overall average	0.0475					

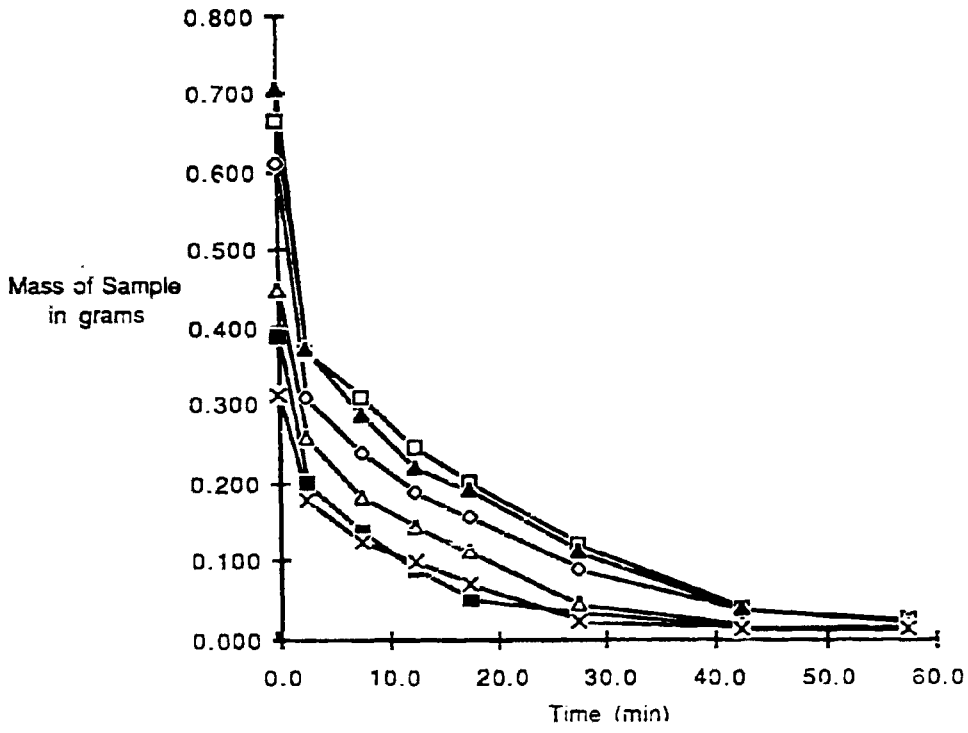

Figure II.F-1. Oxidation of a set of large particles of a Utah Bituminous coal at atmospheric pressure, 1150 K in air. (Platinum crucibles with Mekker burners).

Plans

During the next quarter, the design of the large-particle insert will be completed and fabrication will be initiated. Analytical methods for monitoring the oxidation of large particles will be evaluated. Preliminary experiments with large particles will be continued.

II.G. SUBTASK 2.G. – SO_x/NO_x SUBMODEL DEVELOPMENT

Senior Investigators: L. Douglas Smoot and B. Scott Brewster
Brigham Young University
Provo, Utah 84602
(801) 378-4326 and (801) 378-6240

Research Assistant: Richard D. Boardman

Objectives

The objectives of this subtask are 1) to extend an existing pollutant submodel in PCGC-2 for predicting NO_x formation and destruction to include thermal NO, 2) to extend the submodel to include SO_x reactions and SO_x-sorbent reactions (effects of SO_3 non-equilibrium in the gas phase will be considered), and 3) to consider the effects of fuel-rich conditions and high-pressure on sulfur and nitrogen chemistry in pulverized-fuel systems.

Accomplishments

The first objective of this subtask has been completed. The ability of the Zel'dovich mechanism to match local data was discussed in the 13th Quarterly Report (Solomon et al., 1989d). Figure II.G-1 is repeated here for convenient reference. An evaluation of the thermal NO mechanism sensitivity to reactor and operating conditions has been made to further characterize the thermal NO mechanism. These results are presented in this quarterly report.

Evaluation of the expanded fuel NO mechanism and alternative fuel NO mechanisms has also been completed. The results of this work will be presented in the next quarterly report. Final code integration is currently in progress for the revised/improved NO model.

Work is continuing on the last two objectives. Prediction of gaseous sulfur species has been completed for two entrained-flow gasification cases - one case for North Dakota lignite (low-rank coal) and one case for pressurized gasification of Utah bituminous coal. The results of these predictions are discussed in this report. Plans have been made to complete the SO_x-species/sorbent-reaction submodel during the upcoming quarter.

NO_x Submodel Development

Thermal NO Mechanism Evaluation and Sensitivity Analysis - The BYU/ACERC reactor data collected during this study with independent funding served as a useful benchmark for the Zel'dovich mechanism. Comparisons of predicted NO concentrations with local data were presented and discussed in the 13th Quarterly Report (Solomon et al., 1989c). Subsequently, the model sensitivity to various mechanism options and reactor conditions has been investigated. This analysis included examination of the method used to estimate radical oxygen and the importance of the Zel'dovich mechanism reverse reaction steps. The impact of turbulence on the reaction rates and wall boundary conditions was also determined. Finally, the capability of the model to predict the effects of swirl number and equivalence ratio was systematically investigated to determine the utility of the code for predicting thermal NO in gas-fired burners. In the absence of gas/particle interactions and heterogeneous processes, a greater understanding of the predictive technique has been accomplished.

Rate Expression Form - The extended Zel'dovich mechanism was discussed in previous quarterly reports along with rate expression derivations and studies conducted to measure the rate constants. Here, it is sufficient to present the equations that are useful for modeling NO formation. The general rate expression which includes the forward and reverse reactions in the three-step extended Zel'dovich mechanism is:

$$\frac{d[NO]}{dt}=2[O]\left\{\frac{k_1[N_2]-\frac{k_{-1}k_{-2}[NO]^2}{k_2[O_2]}}{1+\frac{k_{-1}[NO]}{k_2[O_2]+k_3[OH]}}\right\}, \text{gmole cm}^{-3}\text{s}^{-1} \qquad \text{(II.G-1)}$$

A simplified expression is obtained by assuming initial concentrations of NO and OH are low so that only the forward rates of the Zel'dovich mechanism are significant.

$$\frac{d[NO]}{dt}=2k_1[O][N_2], \text{gmole cm}^{-3}\text{s}^{-1} \qquad \text{(II.G-2)}$$

Both rate equations are coupled to the fuel oxidation process through competition for the oxygen radicals. In fuel-lean, secondary combustion zones, where CO is oxidized to CO_2, oxygen atoms are often assumed to be in equilibrium with O_2.

$$O_2 + M \leftrightarrow 2O + M \qquad \text{(II.G-3)}$$

In the flame region where hydrocarbons are consumed, oxygen concentrations often exceed the level which is predicted by Eq. (II.G-3). Schott (1960) hypothesized that O and OH radical concentrations may be approximated by assuming the bimolecular reactions,

$$H + O_2 \leftrightarrow OH + O \qquad \text{(II.G-4)}$$

$$O + H_2 \leftrightarrow OH + H \qquad \text{(II.G-5)}$$

$$OH + H_2 \leftrightarrow H_2O + H \qquad \text{(II.G-6)}$$

equilibrate prior to removal of radicals by relatively slower three-body recombination reactions that lead to full equilibrium. In addition to the fast-shuffle oxy-hydrogen reactions, Kaskan (1956) postulated that partial equilibrium is also approached in fuel-rich regions of gaseous hydrocarbon flames where CO is further oxidized to CO_2:

$$CO + OH \leftrightarrow CO_2 + H \qquad \text{(II.G-7)}$$

Combining equilibrium expressions for the reactions in Eqs. II.G-3 and 6 yields a "quasi equilibrium" expression, explicit only in predictable major species, to estimate radical oxygen concentrations.

$$[O] = K_{eq} \frac{[O_2][CO]}{[CO_2]} \qquad \text{(II.G-8)}$$

Several investigators used Eq. II.G-2 to predict NO formation (e.g. Sarofim and Pohl, 1973; and Drake et al., 1987). A comparison of both rate expressions was made in order to rationalize using Eq. II.G-2, which is computationally more stable. For the benchmark case presented in Figure II.G-1, a difference of less than one ppm NO was predicted (29.6 ppm vs. 28.8 ppm) assuming oxygen radicals are in partial equilibrium with molecular oxygen.

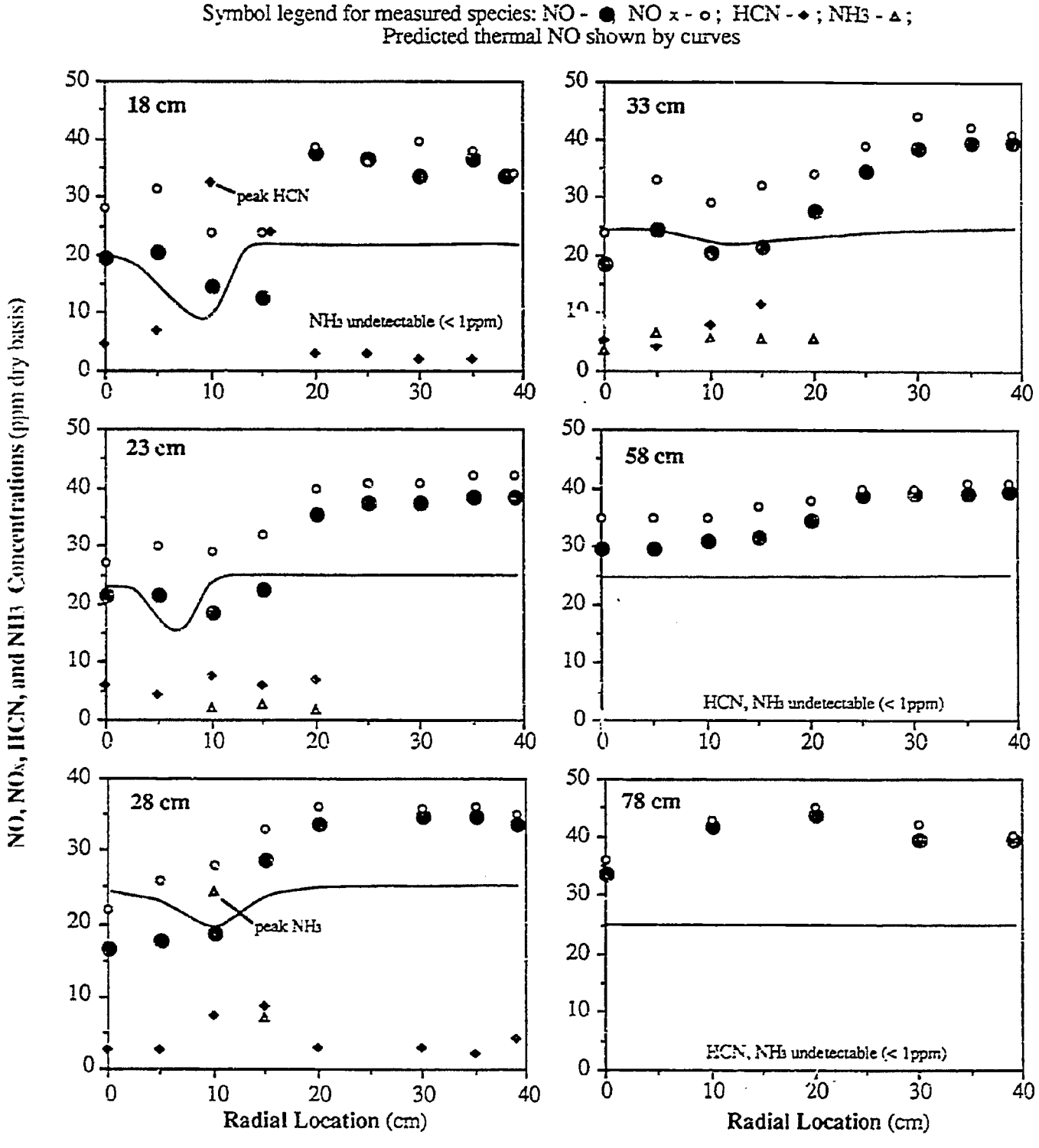

Figure II.G-1. Comparison of predicted thermal NO with measured NO for a natural gas/air diffusion flame. Axial locations listed in upper left corner. Data measured in the BYU/ACERC reactor. E.R.=0.98; Secondary air swirl = 1.5. HCN, NH_3, NO_x data also shown.

Thus, little difference in the predicted solutions was observed for a near-stoichiometric air-to-fuel ratio. This conclusion may not apply to fuel-rich stoichiometries where the concentrations of OH radicals is high. When OH concentrations are greater than 0.1 mole percent (i.e. 1000 ppm) then the assumption of low OH concentrations is no longer valid and Eq. II.G-1 should be used unless numerical instabilities are encountered.

Figure II.G-2 shows the large variation in predicted NO due to the method used to predict radical oxygen concentration. Both curves were calculated using the prescribed expressions for estimating radical oxygen concentration at all locations throughout the reactor. The temperature-dependence was determined by globally adjusting the predicted temperature profile by the amount shown on the abscissa, holding the major species concentrations constant. The sensitivity to gas temperature verifies the expected sensitivity of the NO model to temperature. It has been previously demonstrated that both predicted and measured fuel NO concentrations are temperature-insensitive (Boardman, 1988). The substantial increase in predicted thermal NO concentrations at all temperatures shown by the upper curve reveals that Eq. II.G-8, should not be used to estimate oxygen concentration for all stoichiometries. In general, it may only be valid in extremely fuel-rich regions as will be demonstrated presently.

Fenimore (1971) concluded that the growth of NO in the post-flame gas of ethylene, methane, and propane flames, after hydrocarbons are consumed, can be predicted assuming equilibrium between atomic and molecular oxygen; however, a faster NO formation rate in the primary reaction zone was not accurately described. Rapid NO formation near the combustion zone was later shown to be predictable when the overshoot in radical O and OH concentrations was estimated (Thompson et al., 1981; and Sarofim and Pohl, 1973). Over the past decade, a clearer understanding of the increased NO rates in the flame zone has been obtained (Morley, 1981; Hayhurst and Vince, 1983; Chen et al., 1981; Hayhurst and Vince, 1983; Miller and Bowman, 1989). The importance of prompt NO and the effect of radical concentrations in excess of their equilibrium values have both been demonstrated.

In the present work, prompt NO formation was evident by detection of HCN in the near-burner region on the fuel-rich side of the flame edge (see Figure II.G-1). It may also be expected that some of the NO formed will be destroyed by HCN and NH_3 in the fuel-rich recirculation zone. Without a comprehensive kinetic model, the effect of these reactions cannot be quantified. Figure

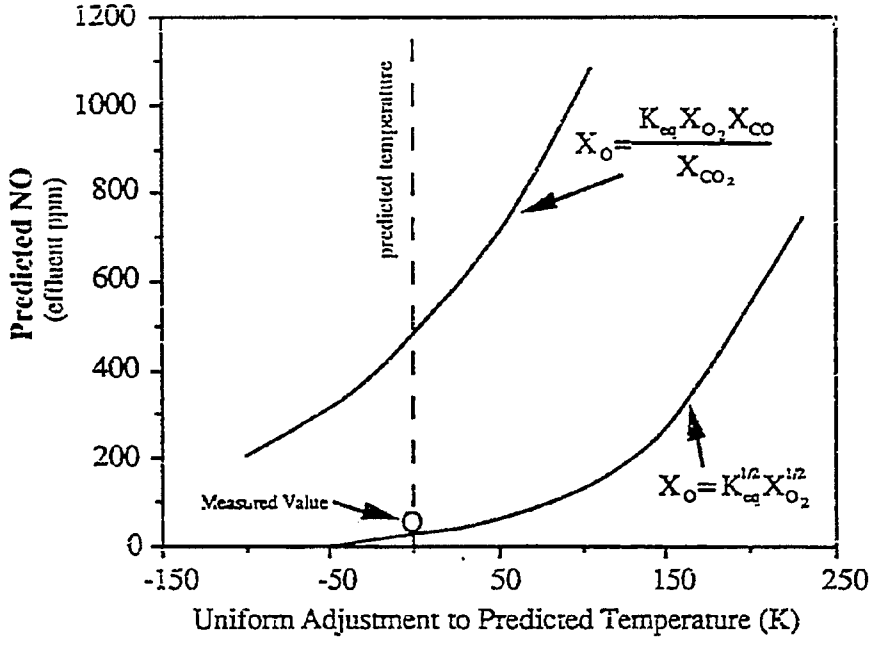

Figure II.G-2. Sensitivity of predicted NO to temperature and the method used to estimate radical oxygen for the bench mark case (ACERC reactor, S.N.=1.5, E.R.=0.98).

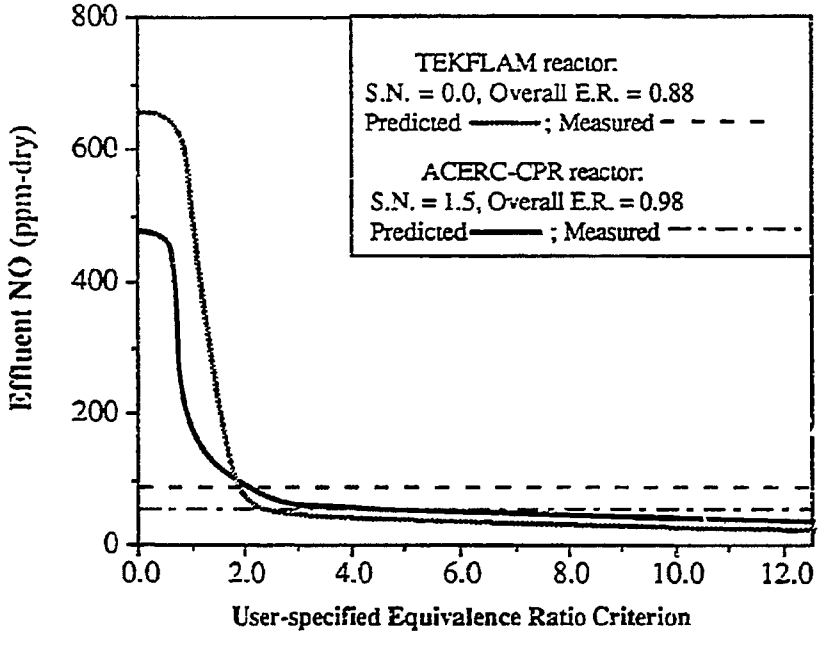

Figure II.G.-3. Sensitivity of predicted effluent NO concentration to method used to estimate local radical oxygen concentrations. When the local equivalence ratic is less than the user-specified criterion, Eq. II.G.3 is used to esimate radical oxygen. When the local equivalence ratio is greater than this criterion, Eq. II.G-8 is used to calculated local radical oxygen concentration. Solid curves show the predicted effluent value that is predicted for any criterion. Dashed lines show the measured effluent concentration. The intersection of dashed and solid curves reveals the equivalence ratio criterion for which the theory matches the measurments for the two cases illustrated.

II.G-2 demonstrates that NO concentrations are grossly overpredicted when Eq. II.G-8, which is valid only for fuel-rich regions, is used to estimate O concentrations throughout the entire reactor.

PCGC-2 predicts the local equivalence ratio at each grid node in the reactor. In diffusion flames, the equivalence ratio varies from zero (pure oxidizer) to infinity (pure fuel). A scheme was developed to allow the code to check the local equivalence ratio at each node in the computational domain and choose either Equation II.G-3 or Equation II.G-8 to estimate the radical oxygen concentrations depending on some criterion specified by the user. The user may specify any arbitrary equivalence-ratio criterion which is compared to the predicted local equivalence ratio at each node during the computation run. Whenever the predicted equivalence ratio is less than the specified criterion, the local radical oxygen concentration at a node is estimated by Equation II.G-3; otherwise, Equation II.G-8 is used. Thus, in local regions where the stoichiometry is sufficiently fuel-rich, radical oxygen concentration is estimated using Equation II.G-8.

Predictions were made in an effort to determine which particular equivalence-ratio criterion gives the best agreement with the experimental data. Predicted effluent NO concentration is plotted in Figure II.G-3 for two separate cases. The asymptote of each curve, as the criterion approaches zero, gives the predicted effluent NO value when radical oxygen concentration is predicted by Equation II.G-8 at every node in the reactor. The asymptote of the curves, as the test parameter becomes large, gives the predicted effluent NO concentration when Equation II.G-3 is used to predict radical oxygen, regardless of the local equivalence ratio.

One important observation that is made from Figure II.G-4 is that the predicted effluent NO concentration matched the experimental measurements when the local equivalence ratio test criterion was approximately 2.0 for the TEKFLAM reactor case and 4.0 for the ACERC reactor case. The large variation in predicted effluent NO concentration over a narrow range of the equivalence ratio test criterion shows that it is not possible to specify a single criterion which is universal for all cases and fuel types. In fact, the equivalence ratio test criterion is likely to be both case- and fuel-specific.

These results indicate that Equation II.G-3 is the preferred choice for estimating radical oxygen concentration throughout the entire reactor when thermal NO concentration is to be predicted a priori. There may still be some

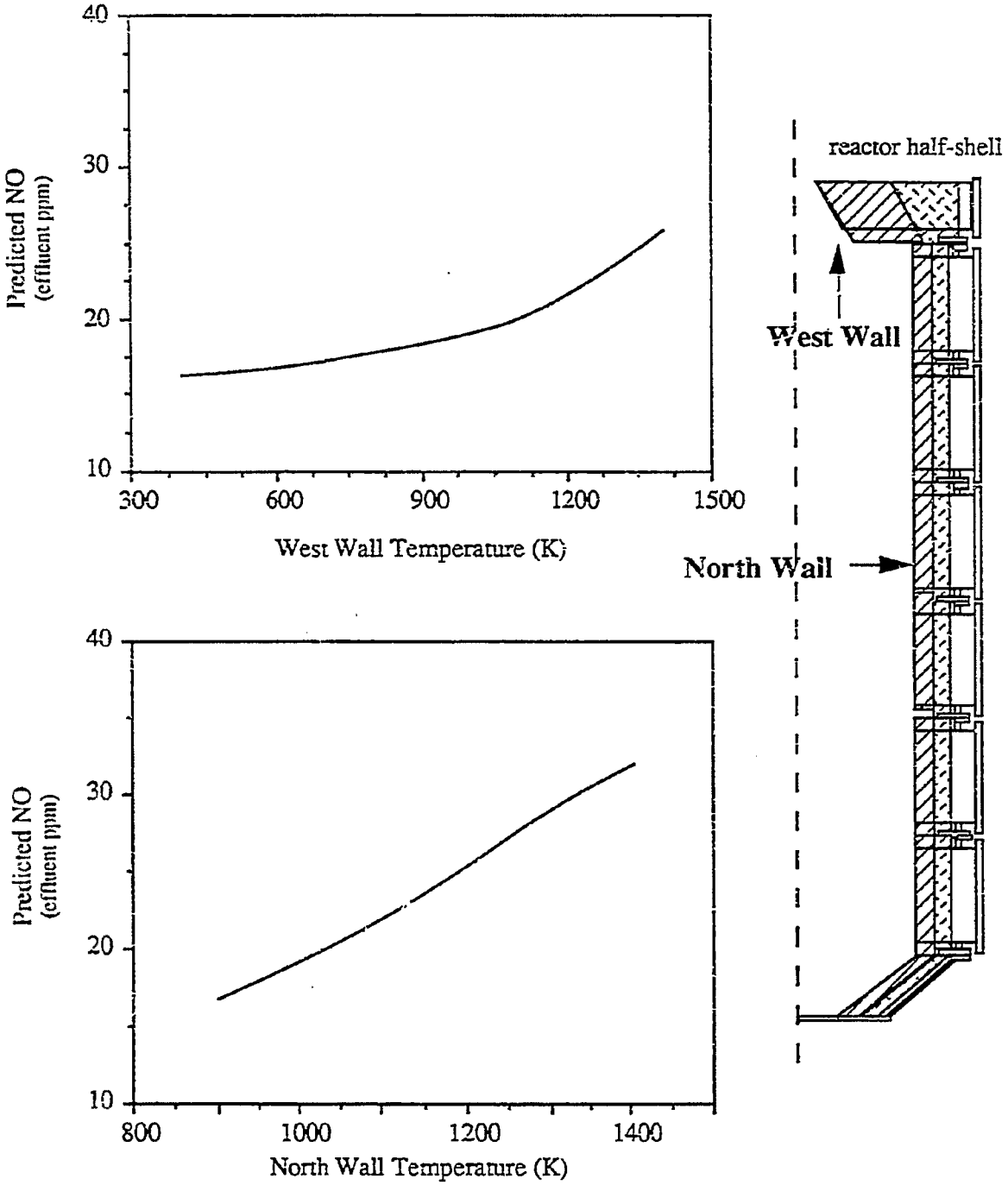

Figure II.G-4. Sensitivity of predicted NO concentrations to variation in specific wall temperatures holding the adjacent walls at 1000 K for the bench mark case (ACERC reactor, S.N.=1.5, 500,000 Btu/hr natural gas/air diffusion flame, E.R.=0.98).

value to the equivalence-ratio criterion when limited experimental data are available and knowledge of detail local NO concentrations are desired. If the sparse NO measurements can be more closely matched by judicious selection of the equivalence ratio test parameter, then the entire field of NO_x concentration presumably will be more correct. This illustrates the synergism that may be realized by joint theoretical and experimental low-NO_x burner design studies.

Wall Temperature Variation - The sensitivity of the thermal NO predictions to wall boundary temperatures was determined by systematically adjusting single wall temperatures over several hundred degrees while maintaining all other wall boundaries at 1000 K. The results plotted in Figures II.G-4 demonstrate significant sensitivity to wall temperature. This was attributed to a proportional increase in the local gas flame temperature due to convective and radiative heating from the hotter walls. Increasing the north wall temperature is shown to effect NO formation the most for the benchmark case, giving rise to a 100 percent increase in NO concentration over a wall temperature increase of 400 K. The west wall (or inlet wall) affected NO formation less, but still caused a 50 percent increase in NO concentration over the same temperature range (T_w = 900 to 1400) This is a significant result since it demonstrates the impact of radiation on NO concentration. Recently, Turns and Lovett (1990) showed that radiation losses from the flame zone have a measurable effect on NO formation. The demonstrated sensitivity of NO formation suggests the importance of investigating the effects of radiation/turbulence interactions on NO chemistry and perhaps the fuel oxidation kinetics as well.

Turbulence Interactions - The sensitivity of the thermal NO rates to turbulence interactions was found to be significant. Figure II.G-5 shows that the predicted effluent NO concentration is 400 percent lower when mean rates are calculated using the local average temperature and species concentrations. Nitric oxide concentrations were 600 percent greater when chemistry/turbulence interactions were taken into account for a pulverized coal case (where convolution is made over the joint probability of primary gas and coal off-gas, (Hill, 1984). Both observations demonstrate the importance of accounting for turbulence/chemistry interactions when predicting nitrogen pollutants in turbulent combustors.

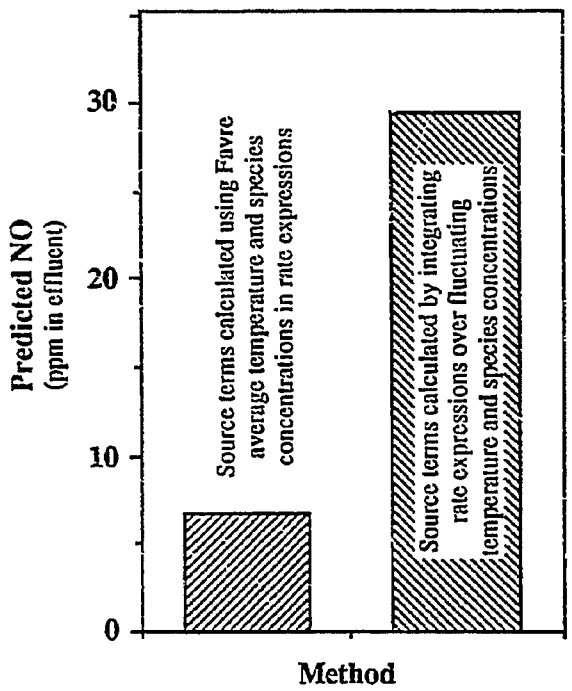

Figure II.G-5. Sensitivity of predicted NO concentrations to turbulent fluctuations for the bench mark cases (ACERC reactor, 500,000 Btu/hr natural gas/air diffusion flame, S.N.=1.5, E.R.=0.98).

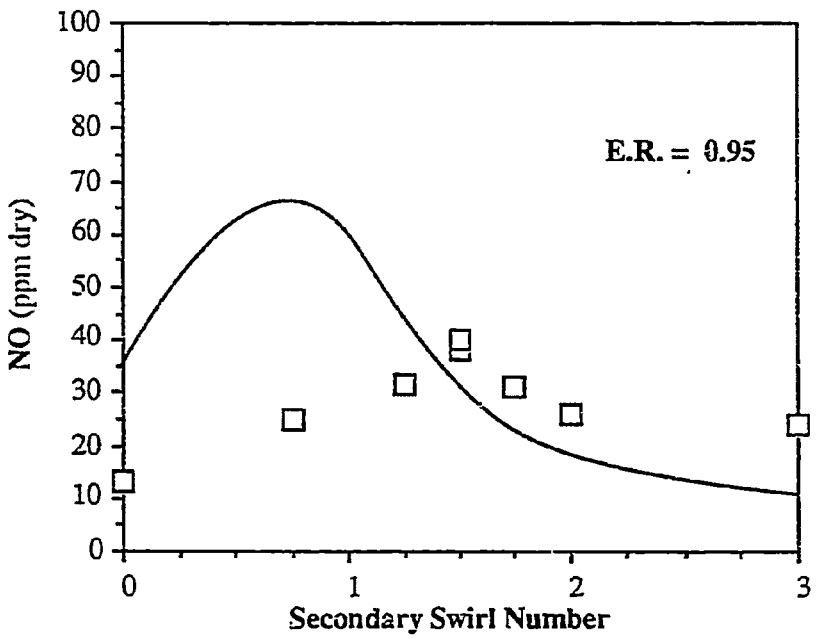

Figure II.G-6.Comparison of predicted (curve) and measured (symbols) NO concentrations for systematic variation in secondary swirl number holding equivalence ratio constant. Data measured in the BYU/ACERC reactor for a 500,000 BTU/hr natural gas/air diffusion flame.

Adjustments to Burner Design Parameters

As more utilities convert from coal to natural gas for their primary fuel, in the wake of less expensive natural gas and the increasing burden of reducing NO_x emissions in coal-fired boilers, the need to retro-fit existing furnaces with advanced technology persists. A great deal of interest continues in research and development of low-NO_x burners. Practical experience has demonstrated that NO_x emissions can be effectively reduced when the burner is aerodynamically staged. The two variables that can be easily adjusted to accomplish staged conditions are the burner equivalence ratio and inlet swirl. The greatest utility of the NO model would be realized if the code can match trends that relate to practical burner design parameters. In the current study, investigation of the effects of secondary-air swirl number and overall equivalence ratio were systematically investigated in the BYU/ACERC reactor.

Swirl Number Variation - Flame stabilization is accomplished by imparting swirl to the secondary inlet stream. An extensive review of modeling swirl in turbulent flows is given by Sloan et al., (1986). The formation of NO_x is impacted by the degree of swirl due to the effects of enhanced turbulent mixing and recirculation characteristics of the flow field. For any rate-limited model, the reaction progress is governed by the time that reactants are associated at a local point. In the following discussion all reference to swirl number will refer to secondary swirl holding the primary stream inlet in straight-pipe flow.

The observed effects of swirl on final NO emissions are varied and depend on parameters other than secondary swirl number alone. The experimental NO data presented in Figures II.G-6 and II.G-7 from the BYU/ACERC reactor and the TEKFLAM experiments illustrate this point. The major difference between cases is the burner geometry dimensions. The TEKFLAM reactor primary tube diameter is one-half the diameter of the BYU reactor (1.4 cm vs 2.7 cm). This leads to a significantly higher primary velocity (~30 m s^{-1} vs ~12 m s^{-1}). Turns and Lovett (1990) showed a direct correlation between NO_x emissions and primary-jet velocities for non-swirling flows over a similar range of primary jet Reynolds number (Re = 10,000-60,000). In general, increasing primary stream inlet velocity changes the flame character and increases NO_x concentration indices. While PCGC-2 predicts the flow field

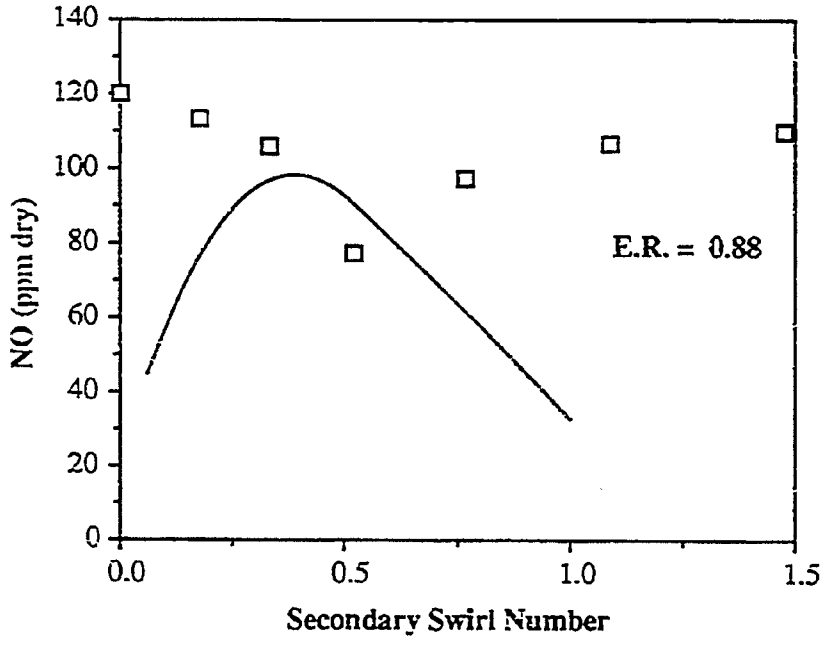

Figure II.G-7. Comparison of predicted (curve) and measured (symbols) NO concentrations for systematic variation in secondary swirl number holding E.R. constant. Data measured in the TEKFLAM reactor (Kolb, 1989) for a 500,000 BTU/hr natural gas diffusion flame.

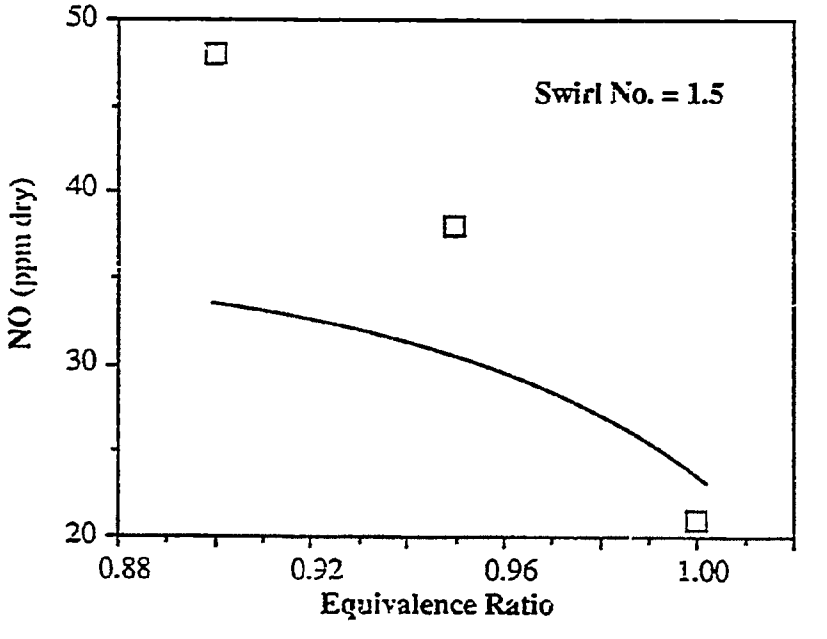

Figure II.G-8. Comparison of predicted (curve) and measured (symbols) NO concentrations for systematic variation in equivalence ratio number holding swirl constant. Data measured in the BYU/ACERC reactor for a 500,000 BTU/hr natural gas diffusion flame.

correctly for changing primary velocity, the NO_x submodel does not predict the variation in trends.

When secondary swirl is introduced, NO_x emissions may either increase or decrease as shown by the experimental data in Figures II.G-6 and 7, respectively. NO_x concentration measured in the BYU reactor increases with increasing swirl number and passes through a local maximum at a swirl number of 1.5. An opposite trend was observed in the TEKFLAM experiments.

NO model computations were made to investigate the capability of predicting the influence of swirl number. The predicted and measured NO concentrations for the separate reactor cases are plotted by the smooth curves in Figures II.G-6 and 7. Figure II.G-6 shows qualitative agreement between the theory and experimental data. The predicted maximum NO concentration was 50 percent higher than the peak experimental value, and occurred at a swirl number of 0.75 instead of 1.5. A similar comparison between the measured data and model predictions was made for other equivalence ratios.

Figure II.G-7, does not show favorable comparison to either the trend or magnitude of the data measured in the TEKFLAM reactor. In fact, the predicted results are similar to those illustrated in Figure II.G-6. Therefore, the impact of primary velocity on NO emissions was not properly predicted. The trend in Figure II.G-7 could be predicted when wall temperatures for the low swirl points were adjusted upwards. The impact of wall temperature on NO concentration was discussed previously (refer to Figure II.G-4). Whether the adjustments made in this work were within reasonable limits cannot be determined since little data regarding the temperature profiles were available. The strong sensitivity of the model to boundary wall temperatures may lead to erroneous predictions and the ability to match trends should be further investigated before final conclusions are made.

Equivalence Ratio Variation - Gas flame NO_x concentration has been shown to increase with increasing excess air until the flame temperature begins decreasing as a result of diluent nitrogen. Under extremely lean, relatively low temperature conditions, thermal NO may form through a nitrous oxide intermediate (Miller and Fisk, 1987). In the natural gas experiments conducted in the ACERC reactor, the equivalence ratio was limited to a tight range to avoid any formation of thermal NO through mechanisms other than the Zel'dovich mechanism. Figure II.G-8 compares the NO model predictions to the observed trend. While the trend appears to be qualitatively correct, the

magnitude at lower equivalence ratios (higher stoichiometric air to fuel ratios) does not match the measured magnitude. NO formation via N_2O production is possible. The difference between the predicted and measured local data in Figure II.G-1 could be attributed to a separate thermal NO mechanism that is not included in the NO model. Further conjecture for this hypothesis is shown is Figure II.G-9 since the largest disparities between the Zel'dovich mechanism and measurements occur at the lowest equivalence ratios. The potential for NO formation via N_2O increases with equivalence ratio.

Summary of Thermal NO Mechanism Validation

The limited sensitivity analysis of the Zel'dovich mechanism reveals many inadequacies of the NO model for predicting thermal NO concentrations in practical gas-fired combustors. The relative importance of prompt NO and other reactions (i.e. NO_2 and N_2O chemistry) have not been determined. The impact of wall temperature was found to be significant. Since PCGC-2 requires wall temperature as a specified boundary condition, some caution must be exercised in interpreting NO_x model trends with variables such as swirl in the absence of adequate wall temperature data. The effect of chemistry/turbulence interactions was shown to be especially significant for thermal NO formation, as it had been for fuel NO formation. Finally, considerable sensitivity to the method used to predict radical oxygen concentration was demonstrated.

Notwithstanding the above-mentioned uncertainties and sensitivity, the qualitative agreement shown between the predicted and measured NO concentrations in Figures II.G-1, 6 and 8 demonstrates that the NO model can be employed as a supplementary tool to aid burner design procedures. When coupled with reliable data, its complementary role in gas-fired burner design will be enhanced. However, the absence of a mechanism to describe prompt NO precludes the ability of the code to predict final NO emissions for complex gas-fired burners.

Figure II.G-9 plots the measured NO values against the NO model predictions. The model always predicts the general magnitude of the data for all of the cases shown. The relative difference for the most disparate data points is around a factor of 3. In view of the significant sensitivity to turbulence, wall temperature, radical oxygen concentration, and the absence of other NO formation mechanisms in the model, the comparisons between predictions and measurements are generally favorable.

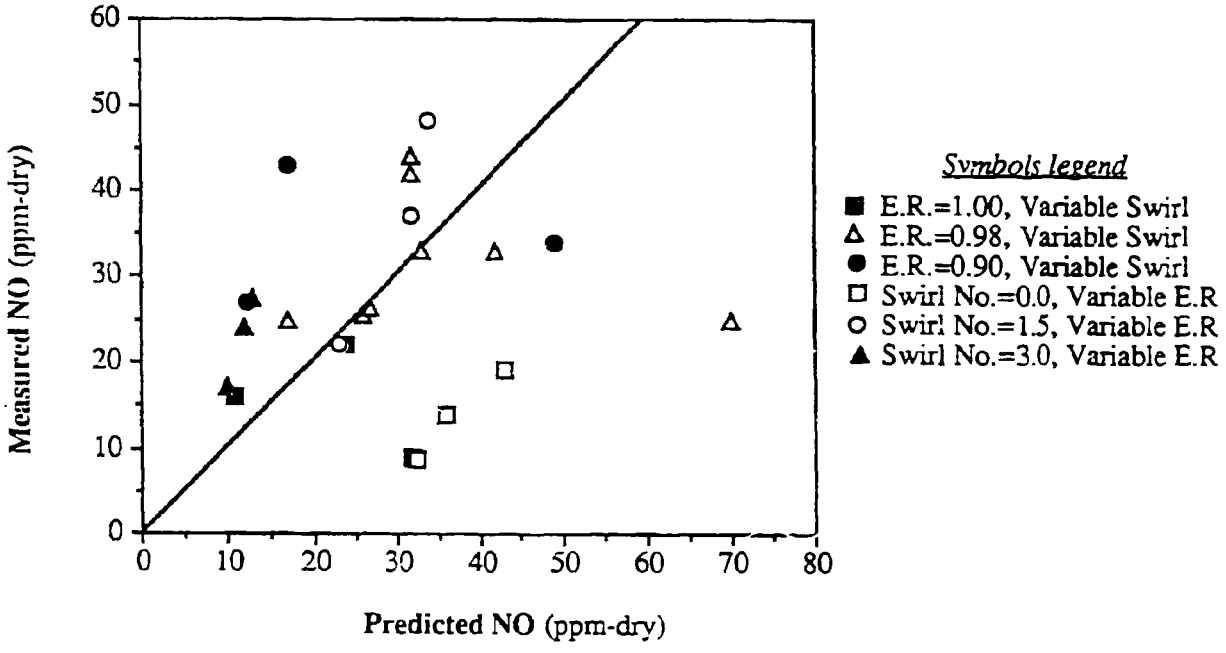

Figure II.G.-9. Scatter plot of predecited versus measued NO concentrations showing general agreement of thermal NO predictions. Measured data from the BYU/ACERC reactor; 500,000 BTU/hr natural gas/air diffusion flame.

Fuel NO Mechanism Evaluation

Predictions for coal combustion and gasification cases have been completed to verify the extended and alternative fuel NO mechanisms that have been incorporated into the revised NO model. The main focus of this model evaluation is to investigate the capability to predict nitrogen pollutant formation during low-rank coal gasification. The relative significance of thermal NO during coal combustion has also been addressed. The results of this work will be presented and discussed in a future quarterly report.

SO_x-Sorbent Reactions Submodel Development

The general framework for a SO_x-species/sorbent-reactions submodel was presented in the 3rd Annual report (Solomon et al., 1989). The proposed method of calculating gaseous sulfur species is to assume instantaneous equilibrium occurs in the gas phase once the sulfur is released to the gas phase. Comparisons of predicted and measured sulfur species (SO_2 and H_2S) for combustion of Utah bituminous coal and Wyoming subbituminous coal were discussed in the 3rd Annual Report. Two additional cases have now been investigated for fuel-rich and pressurized reactor conditions. Figures II.G.10-13 compare SO_2 and H_2S radial profile data for the gasification of Utah bituminous coal and North Dakota lignite.

While there is large scatter among the experimental data, the predicted curves generally follow the magnitude of the measurements for both coal types. Thus, for the development and demonstration of a SO_x-capture submodel, it is felt the current approach to predicting SO_2 and H_2S may be suitable.

Plans

Work during the upcoming quarter will focus on the implementation of a SO_x-species/sorbent-reactions submodel. There are two aspects which remain on this task. First, PCGC-2 will be modified to track the sorbent particles. Second, reaction expressions describing the depletion of H_2S and SO_2 will be incorporated. Subsequent to these details, simulations will be made to demonstrate the performance of the submodel.

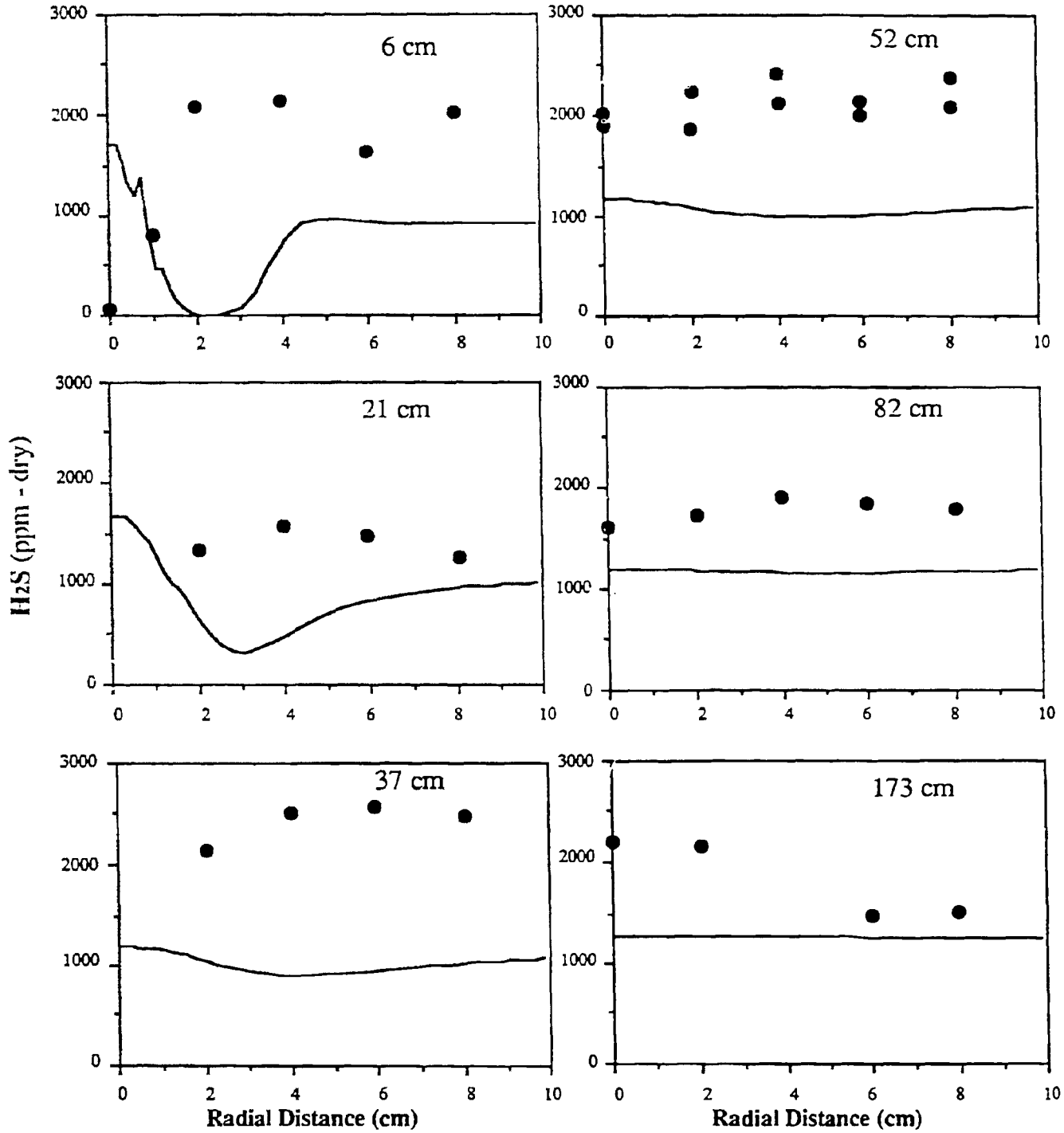

Figure II.G-10. Predicted and measured H_2S concentration for pressurized gasification (5 atm) of Utah bituminous coal.

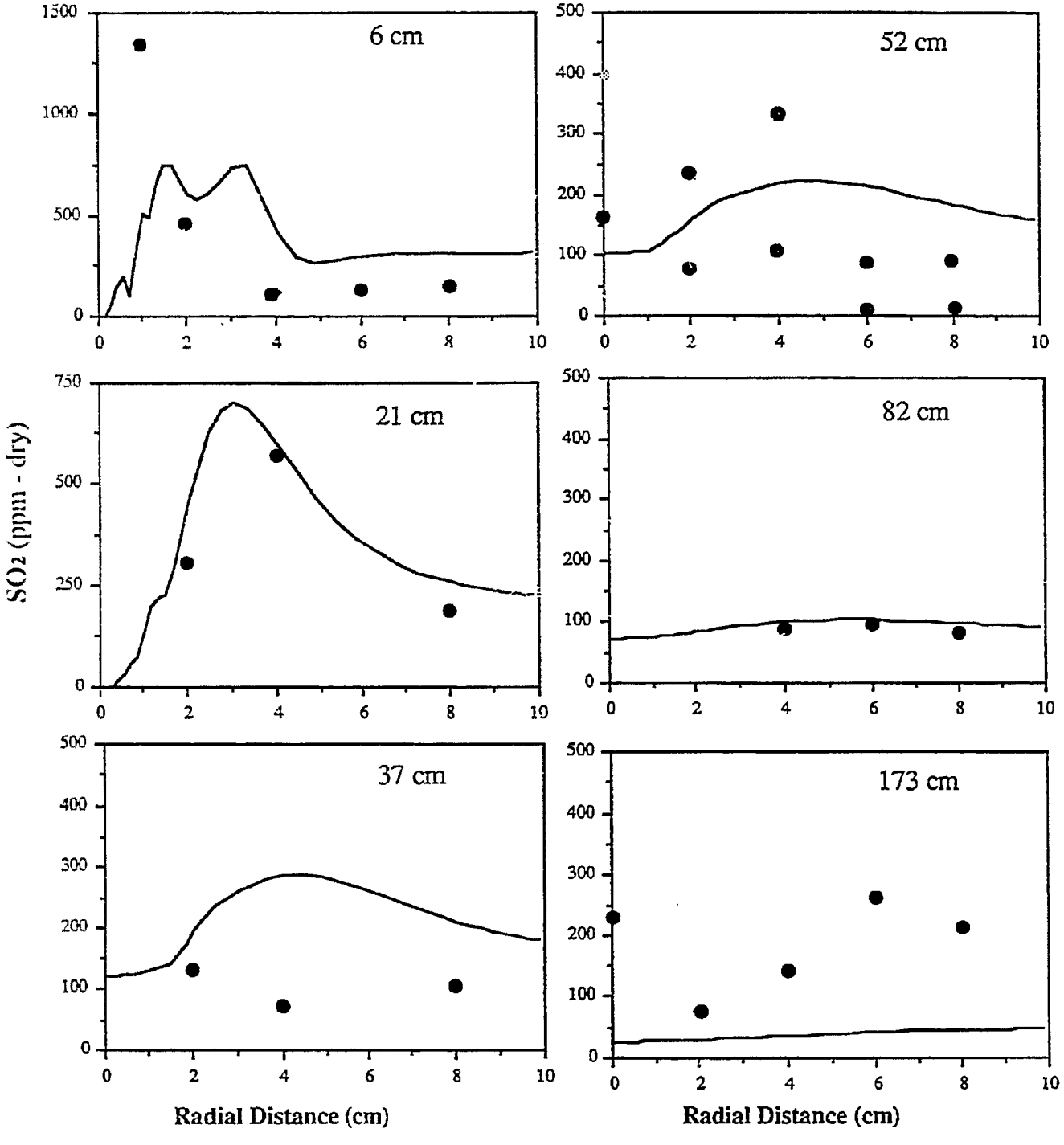

Figure II.G-11. Predicted and measured SO_2 concentration for pressurized gasification (5 atm) of Utah bituminous coal.

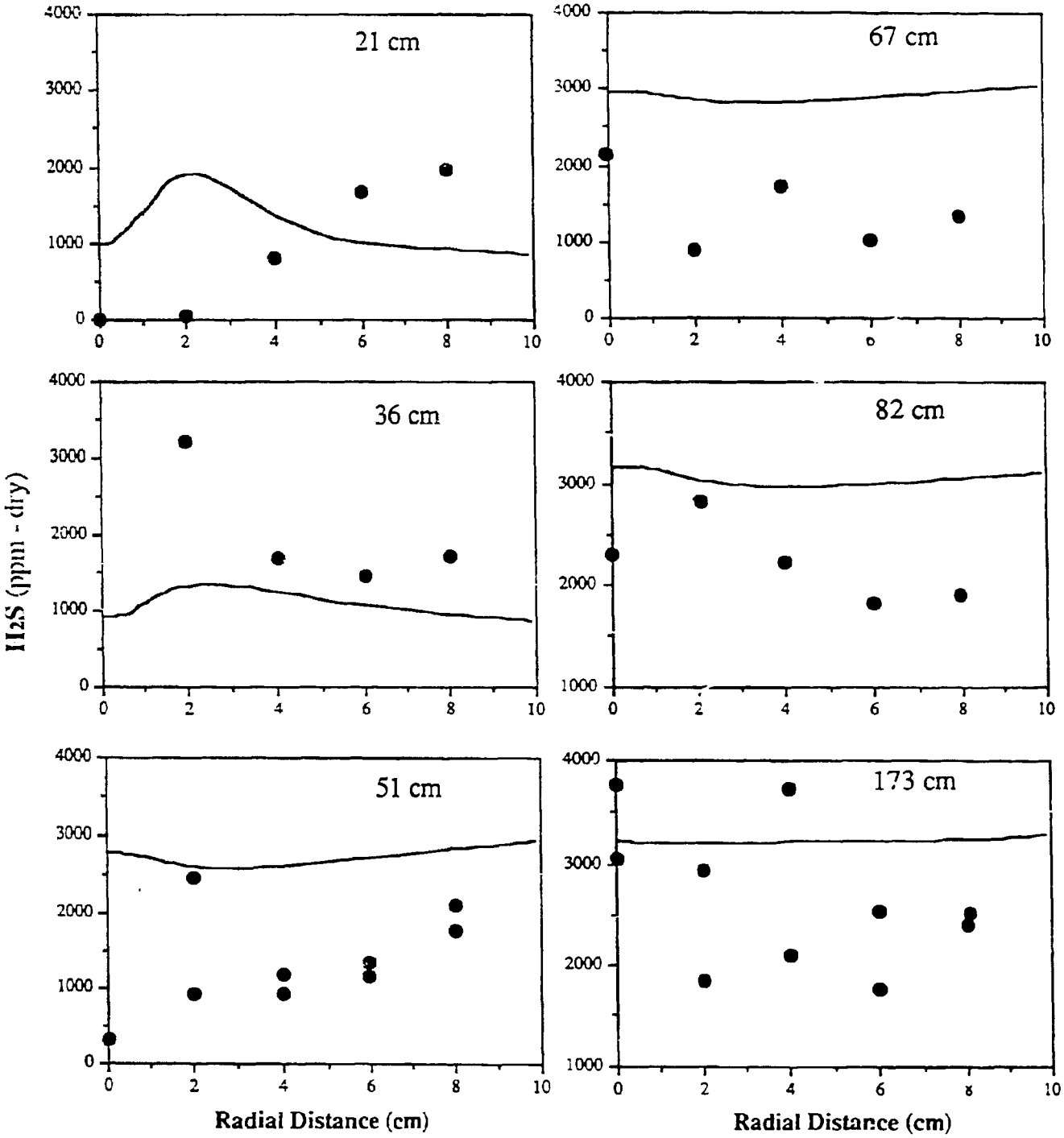

Figure II.G-12. Predicted and measured H_2S concentration for pressurized gasification of North Dakota lignite.

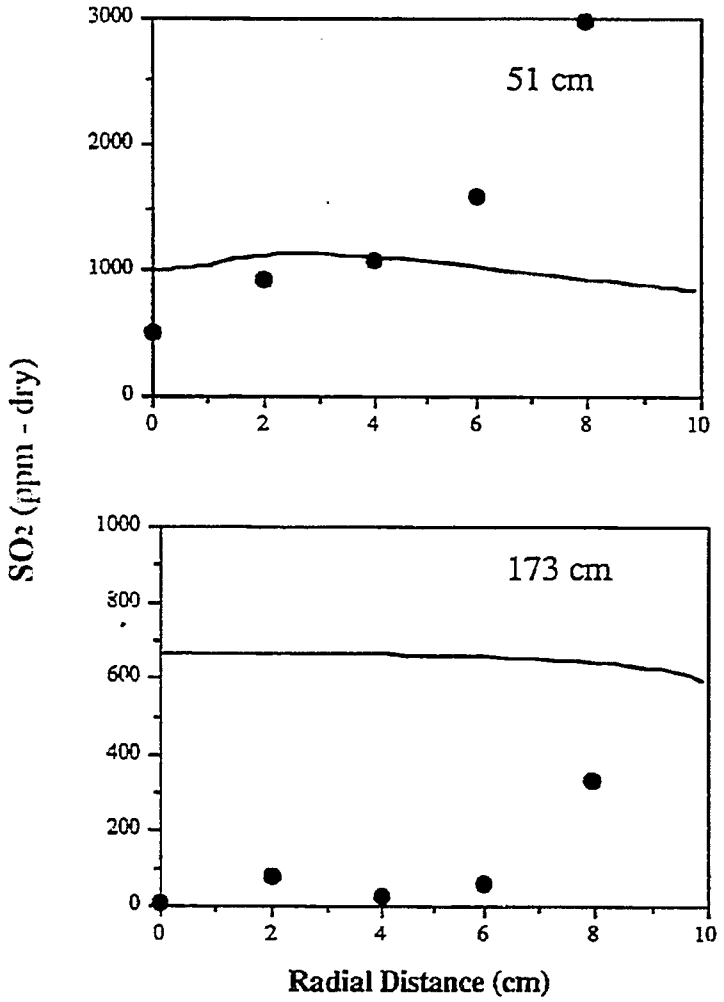

Figure II.G-13. Predicted and measured SO2 concentration for pressurized gasification of North Dakota lignite.